The 50-year Landsat collection 2 archive

Christopher Crawford, David Roy, Saeed Arab, Christopher Barnes, Eric Vermote, Glynn Hulley, Aaron Gerace, Mike Choate, Christopher Engebretson, Esad Micijevic, et al.

Science of Remote Sensing 8 (2023) 100103

Contents lists available at ScienceDirect

Science of Remote Sensing

journal homepage: www.sciencedirect.com/journal/science-of-remote-sensing

The 50-year Landsat collection 2 archive

Christopher J. Crawford [a,*], David P. Roy [b,c], Saeed Arab [d], Christopher Barnes [d], Eric Vermote [e], Glynn Hulley [f], Aaron Gerace [g], Mike Choate [a], Christopher Engebretson [a], Esad Micijevic [a], Gail Schmidt [d], Cody Anderson [a], Martha Anderson [h], Michelle Bouchard [a], Bruce Cook [i], Ray Dittmeier [d], Danny Howard [d], Calli Jenkerson [d], Minsu Kim [d], Tania Kleyians [g], Thomas Maiersperger [a], Chase Mueller [d], Christopher Neigh [i], Linda Owen [d], Benjamin Page [j], Nima Pahlevan [e,k], Rajagopalan Rengarajan [d], Jean-Claude Roger [l], Kristi Sayler [a], Pat Scaramuzza [d], Sergii Skakun [l], Lin Yan [b], Hankui K. Zhang [m], Zhe Zhu [n], Steve Zahn [a]

[a] U.S. Geological Survey (USGS), Earth Resources Observation and Science (EROS) Center, Sioux Falls, SD, 57198, USA
[b] Center for Global Change and Earth Observations, Michigan State University, East Lansing, MI, 48824, USA
[c] Department of Geography, Environment & Spatial Science, Michigan State University, East Lansing, MI, 48824, USA
[d] KBR Contractor to the USGS EROS Center, Sioux Falls, SD, 57198, USA
[e] NASA/Goddard Space Flight Center, Code 619, Greenbelt, MD, 20771, USA
[f] Jet Propulsion Laboratory, California Institute of Technology, Pasadena, CA, 91109, USA
[g] Rochester Institute of Technology, Chester F. Carlson Center for Imaging Science, Rochester, NY, 14623, USA
[h] U.S. Department of Agriculture, Agricultural Research Service, Beltsville, MD, 20705, USA
[i] NASA/Goddard Space Flight Center, Code 618, Greenbelt, MD, 20771, USA
[j] Earth Space Technology Services (ESTS), Contractor to the USGS EROS Center, Sioux Falls, SD, 57198, USA
[k] Science Systems and Applications, Inc., Lanham, MD, 20706, USA
[l] Department of Geographical Sciences, College of Information Studies (iSchool), University of Maryland, College Park, 20742, MD, USA
[m] Geospatial Sciences Center of Excellence, Department of Geography and Geospatial Sciences, South Dakota State University, Brookings, SD, 57007, USA
[n] Department of Natural Resources and the Environment, University of Connecticut, Storrs, CT, 06269, USA

ARTICLE INFO

Keywords:
Landsat
Collection 2
Surface reflectance
Surface temperature
Analysis ready data

ABSTRACT

The Landsat global consolidated data archive now exceeds 50 years. In recognition of the need for consistently processed data across the Landsat satellite series, the U.S. Geological Survey (USGS) initiated collection-based processing of the entire archive that was processed as Collection 1 in 2016. In preparation for the data from the now successfully launched Landsat 9, the USGS reprocessed the Landsat archive as Collection 2 in 2020. This paper describes the rationale for, and the contents and advancements provided by Collection 2, and highlights the differences between the Collection 1 and Collection 2 products. Notably, the Collection 2 products have improved geolocation and, for the first time, the USGS provides a global inventory of Level 2 surface reflectance and surface temperature products. Also for the first time, the USGS used a commercial cloud computing architecture to efficiently process the archive and enable direct cloud access of the Landsat products. The paper concludes with discussion of likely improvements expected in Collection 3 in preparation for the Landsat Next mission that is planned for launch in the early 2030s.

1. Introduction

Landsat 1, launched July 1972, was the first spaceborne digital sensor developed for terrestrial environmental monitoring (Williams and Carter, 1976; Goward et al., 2017) and was followed by a series of improved Landsat sensors that provide the longest, now five-decade, global remote sensing record (Wulder et al., 2022). The design and launch of the Landsat satellites and sensors into near-polar low earth orbit is managed by the National Aeronautics and Space Administration (NASA), and the flight operations, archive, ground processing, and distribution are managed by the U.S. Geological Survey (USGS), with an associated Landsat Science Team serving in a scientific and technical

* Corresponding author.
E-mail address: cjcrawford@usgs.gov (C.J. Crawford).

https://doi.org/10.1016/j.srs.2023.100103
Received 19 July 2023; Received in revised form 6 September 2023; Accepted 13 September 2023
Available online 18 September 2023

evaluation capacity (Roy et al., 2014). Ensuring Landsat mission continuity and so the provision of an uninterrupted global medium resolution satellite record has been a long-standing priority of USGS, NASA, and successive Landsat Science Teams (Roy et al., 2014; Goward et al., 2017; Wulder et al., 2022). The eight Landsat missions (Landsat 1, 2, 3, 4, 5, 7, 8 and 9) provide the longest satellite terrestrial record over a period of substantial human modification of the environment and climate change. The successful 2021 launch of Landsat 9 and provision of U.S. funding for the planned Landsat Next mission (Masek et al., 2020) has secured Landsat mission continuity. However, until the advent of Collection-based processing, the Landsat archive was not processed consistently. This reflected practical cost limitations, the significant changes over the last five decades in satellite, sensor, and ground system technologies, and because Landsat data acquired outside the United States were archived and processed by different agencies.

Conventionally, satellite data are processed into a hierarchy of increasingly refined levels from raw instrument data (Level 0), that are calibrated and geolocated (Level 1), converted into geophysical parameters (Level 2), and gridded, and sometimes temporally composited, into an Earth-based coordinate system (Level 3) (Wolfe et al., 1998). In the first four decades of the Landsat era, most of the imagery acquired outside of the United States were only available from regional and national agencies that downlinked the imagery in their ground station geographic area. In 2010, the USGS began the Landsat Global Archive Consolidation (LGAC) initiative to bring all the raw (Level 0) imagery from these agencies into a centralized global archive located at the USGS Earth Resources Observation and Science (EROS) Center in Sioux Falls, South Dakota (Wulder et al., 2016). The resulting consolidation of the global Landsat archive and the free and open Landsat data access policy that started in 2008 were major steps forward (Zhu et al., 2019) but Landsat data were processed only in response to user requests and so large consistently processed Landsat data sets were unavailable. In addition, the distributed datasets were not atmospherically corrected to reduce scattering and absorption by atmospheric aerosols, gases, and water vapor (Tanré et al., 1990; Tonooka, 2005).

In September 2016, the USGS initiated the first collection-based processing. The archived Landsat 1–8 Level 0 and all newly acquired data were processed to generate Level 1 data that were collectively labelled as Collection 1. Dedicated engineers and scientists undertake routine analysis of recent Landsat acquisitions, and retrospective analysis of Landsat time series, to derive improved characterization of sensor performance (radiometry and geolocation). The Collection 1 processing was undertaken in a consistent manner using the most up-to-date radiometric calibration and to the best achievable geolocation accuracy and, in addition, Level 2 atmospherically corrected products were processed over the conterminous United States (CONUS), Alaska and Hawaii (Dwyer et al., 2018). The success of Collection 1, and several factors, discussed in this paper, including improved geolocation using Landsat 8 harmonized with European Space Agency (ESA) Global Reference Image (GRI) data, new opportunities provided by cloud computing, and the scheduled launch of Landsat 9, meant that the decision was made to process the Landsat data *again* as Collection 2. The main differences between Collection 2 and 1 are summarized in Table 1 and are described in detail later in the paper.

Landsat users can migrate their science and applications to using Collection 2 products since the Collection 1 products were removed from public distribution on December 31, 2022. At the time of writing, Collection 2 is composed of >10.2 million images that occupy >9 petabytes of data collected by the Landsat 1–5 Multispectral Scanner (MSS), Landsat 4 and 5 Thematic Mapper (TM), Landsat 7 Enhanced Thematic Mapper Plus (ETM+), and Landsat 8 and 9 Operational Land Imager (OLI) and Thermal Infrared Sensor (TIRS) sensors. The Collection 2 products include calibrated and geolocated (i) Level 1 top of atmosphere (TOA) heritage ~185 × 180 km images defined in the Universal Transverse Mercator (UTM) projection, (ii) Level 2 surface reflectance and surface temperature images, (iii) for select U.S. regions, analysis ready data (ARD) gridded tiled products defined in the Albers equal area projection. The Collection 2 Level 2 products and U.S. ARD were certified by the Committee on Earth Observation Satellites (CEOS) as being analysis ready data compliant i.e., processed to a minimum set of requirements and organized into a form that allows for analysis with minimal additional user effort that facilitates interoperability with other Earth observation datasets.

Table 1
Summary of main differences between Collection 2 and Collection 1 (the paper section describing the change is shown in parenthesis).

Improved absolute geolocation accuracy using Landsat 8 Operational Land Imager (OLI) harmonized with European Space Agency (ESA) Global Reference Image (GRI) (Section 3.1)
New Digital Elevation Model (DEM) used for orthorectification with improved vertical accuracy (Section 3.1)
Improved radiometric calibration particularly for Landsat 5 and 8 (Section 3.2)
Inclusion of Landsat 9 observations (Section 3.2)
Global coverage Level 2 Surface Reflectance (Section 3.3) and Surface Temperature (Section 3.4) Landsat 4–9 products
Expanded Quality Assessment (QA) bits for Landsat 4–9 (Section 3.5)
Consistent bit design between Level 1 and Level 2 (Section 3.6)
Inclusion of per-pixel solar illumination and sensor viewing geometry (Section 3.6)
Expanded U.S. Analysis Ready Data (ARD) tile grid to cover more of the Aleutian Islands, Great Lakes, and certain coastal regions (Section 3.7)
Improved latency between acquisition and availability of Landsat 8 products (Section 4)
Direct Landsat access and analysis via commercial cloud (Section 4)

This paper overviews the rationale for the Collection 2 processing, improvements over Collection 1, new Collection 2 products, and summarizes Landsat Collection 2 data access. The paper concludes with a discussion of improvements expected in the Landsat Collection 3 processing, a data stream that will include products from the planned follow-on Landsat Next mission.

2. Landsat collection 2 motivation, products and processing overview

Collection-based processing was a significant change in the management of the Landsat archive. Previously, Landsat Level 1 data were processed on demand in response to user and agency orders (Goward et al., 2017). Unfortunately, this meant that different (or the same) users could order the same image acquisition from the global archive on different dates and the processing software, geolocation and calibration used to generate the Level 1 image could be different. In 2008, the USGS officially announced free access to the Landsat archive which accelerated uptake, particularly for large area and multi-decadal analyses (Wulder et al., 2019). As Landsat usage increased, concern over processing inconsistencies led to the recommendation by the Landsat Science Team to process all Landsat data consistently to facilitate generation of traceable, quality, higher-level science and application information products (Roy et al., 2014). In recognition of the need for consistently processed data, the USGS initiated collection-based Landsat processing emulating the NASA Moderate Resolution Imaging Spectroradiometer (MODIS) land product collection numbering approach (Justice et al., 2002). The first Collection 1 Landsat processing was undertaken to generate a consistently processed version of the archive, while recognizing that future reprocessing would occur to reflect improved sensor calibration and geolocation knowledge as well as feedback from the user community (Dwyer et al., 2018).

Within the USGS Landsat program and the Landsat Science Team, the undesirability of producing a new collection too soon after the previous one was discussed. It is well established that there should be sufficient time for users to become familiar with a new collection, and several years of collection data are needed typically to characterize the data quality, particularly of Level 2 and 3 products (Masuoka et al., 2011). Further, collection-based processing is not inexpensive, as both the archived and all newly acquired data must be processed and copying a

Landsat collection to another institution (such as a cloud hosting service, national agency or well-resourced academic research group) is non-trivial. After assessing these constraints, the Collection 2 processing was initiated in September 2020.

The Collection 2 processing was motivated primarily by the ability to improve the Landsat absolute geolocation accuracy using Landsat 8 geolocational imaging performance harmonized with the ESA GRI data (Section 3.1). In addition, new opportunities provided by the availability of commercial cloud computing meant that efficient processing of the archived data to include global Level 2 surface reflectance (Section 3.3) and surface temperature (Section 3.4) products was possible. This also meant that the Collection 2 products could be stored in the cloud to provide new cloud-based analysis opportunities without the need for users to download Landsat data to their institutions. The schedule of the Collection 2 processing was driven by the planned launch of Landsat 9 (Masek et al., 2020) because of the desirability of processing the newly acquired Landsat 9 imagery as part of a new collection. Landsat 9 launched successfully, after a short delay, in September 2021.

The Collection 2 Level 1 and Level 2 products have the same geometry and are provided with a similar format as Collection 1 in approximately 185 km × 180 km images defined in the Universal Transverse Mercator (UTM) projection, or in the Polar Stereographic (PS) projection over polar regions. The image locations are referenced, as for Collection 1, by the Worldwide Reference System (WRS) path and row coordinates. The Collection 2 Level 1 products are generated by projecting the geolocated (Section 3.1) and radiometrically corrected (Section 3.2) Level 0 data into the UTM or PS projection. Top-of-atmosphere (TOA) digital numbers (DN) are stored for each spectral band and pixel, with band specific metadata to enable conversion of the DNs to radiance (Wm^{-2} sr^{-1} μm^{-1}) and conversion of the reflective wavelength DNs to reflectance (unitless) and the thermal infrared wavelength DNs to brightness temperature (Kelvin). The Level 2 products are derived from the Level 1 TOA radiance and include surface reflectance (unitless) defined for each reflective spectral band and an estimate of the surface temperature (Kelvin) from TIR wavelengths (Sections 3.3 and 3.4). Unlike for Collection 1, the Collection 2 Level 2 products are provided with global coverage. The Landsat U.S. analysis ready data (ARD) products are generated, as for Collection 1, over the conterminous United States (CONUS), Alaska, and Hawaii for the Landsat 4–9 30 m record (Dwyer et al., 2018). The Collection 2 U.S. ARD are generated by projecting the Level 0 data to the Albers equal area projection, applying the Collection 2 Level 1 and 2 processing algorithms, and then gridding the results into fixed non-overlapping tiles (Section 3.7).

The Collection 2 processing was undertaken using a hybrid on-premises and commercial cloud architecture to enable efficient processing. Previously, the Collection 1 processing was undertaken solely on-premises at the USGS EROS using the Landsat Product Generation System (LPGS). The LPGS was developed in the Landsat 7 era and refined to provide a modular and scalable architecture to which additional storage and processing nodes could be added to increase capacity and performance (Goward et al., 2017; Loveland and Dwyer, 2012). However, the large volume of the Landsat archive and the offering of global Level 2 products meant that timely processing of Collection 2 was not possible using the on-premises LPGS. For Collection 2, the archived Landsat data acquired up to June 2020 were processed in the Amazon Web Services (AWS) commercial cloud and only the newly acquired Landsat 8 and 9 data from June 2020 onwards were LPGS processed on-premises at the USGS EROS. A range of existing AWS tools were used to containerize the LPGS ingest and science processing workflows, data management, and security, and were parallelized to provide efficiencies not achievable using the on-premises LPGS. The Collection 1 Level 1 processing took approximately 18 months to complete using the on-premises LPGS. In contrast, the Collection 2 processing of more than twice the data volume (due to additional processing of the global Level 2 products and another approximately three and half years of Landsat 7 and 8 observations) took five weeks in AWS. The effective processing rates for Collection 1 and 2 were equivalent to processing about 25,000 and 450,000 Landsat images per day, respectively. The Collection 2 products are stored in the Landsat AWS Simple Storage Service (S3) cloud bucket and users can obtain them directly from AWS or using conventional USGS interfaces that are transparent to the AWS storage (Section 4). The Collection 2 Landsat 8 and 9 data generated on-premises at USGS EROS from June 2020 onwards are copied to the AWS S3 cloud and a rolling cache of the previous 90 days of processed acquisitions are retained at the USGS EROS to facilitate near-real time and bulk data access through a machine-to-machine (M2M) application programming interface (API).

3. Landsat collection 2

3.1. Collection 2 improved landsat geolocation

The Landsat geolocation is derived using a geometric sensor model, satellite ephemeris and attitude information, a Digital Elevation Model (DEM), and a library of ground control chips (Storey et al., 2019). The Landsat data are processed to Level 1 with the highest achievable geolocation accuracy - listed with increasing accuracy as L1GS (no DEM or ground control available), L1GT (terrain corrected using a DEM and no ground control), and L1TP (terrain corrected with ground control). Over the 50-year Landsat record, the availability and quality of the satellite ephemeris and attitude information has been variable, particularly for earlier Landsat sensors, and the geolocation is limited by atmospheric cloud obscuration that precludes image matching with the ground control chips (Yan and Roy, 2021). Prior to Landsat 8, the ground control chip library was extracted from orthorectified Landsat 7 ETM + images acquired as part of the Global Land Survey 2000 (GLS-2000) global cloud-free image data set (Gutman et al., 2013). The Landsat 8 OLI pushbroom sensor design and operational onboard global positioning system (GPS) provides improved geometric knowledge compared to previous Landsat missions and the imaged OLI data revealed errors in the GLS-2000 ground control chip library (Storey et al., 2016). The Landsat ground control library was refined using Landsat 8 OLI image chips harmonized to the ESA Sentinel-2 10 m GRI coordinates and is now used in the Collection 2 geometric processing. This involved updating over 5.1 million chips as well as the extraction of 2.5 million new Landsat 8 chips globally for inclusion in Collection 2 (Storey et al., 2019; Rengarajan et al., 2020). In addition, a new DEM is used in Collection 2 that was derived using more recent publicly available elevation data sources (Franks et al., 2020).

Fig. 1 summarizes the typical geolocation differences between the Collection 1 and Collection 2 Level 1 data for Landsat 4–8. The root-mean-square difference (RMSD) (derived as the square root of the sum of the squared mean longitude and mean latitude geolocation collection shifts) scaled to meters defined at each global Landsat WRS-2 path/row are shown. The offsets were computed by averaging the offsets of all ground control chips within a given path/row and based on adjustments undertaken by a block triangulation solution (Storey et al., 2019). In general, most images have sub-pixel (<30 m) geolocation differences between Collection 1 and 2. There are negligible differences over Australia because the ground control library across the continent was improved in time for the Collection 1 processing (Storey et al., 2019). At certain Landsat path/rows, the geolocation differences between collections can be > 30 m (orange and red tones) indicating a significant improvement in the geolocation. Fig. 2 shows an example extracted over path 125/row 43 in China which has a 44.81 m RMSD and illustrates qualitatively the impact of the Collection 1 to 2 geolocation improvement on the reflectance data.

The geolocation accuracy of the Collection 2 Level L1TP imagery is reflected in metadata available with each image. Specifically, the root-mean-square errors (RMSE) between the known ground control and sensed image locations are provided resolved in the Easting and

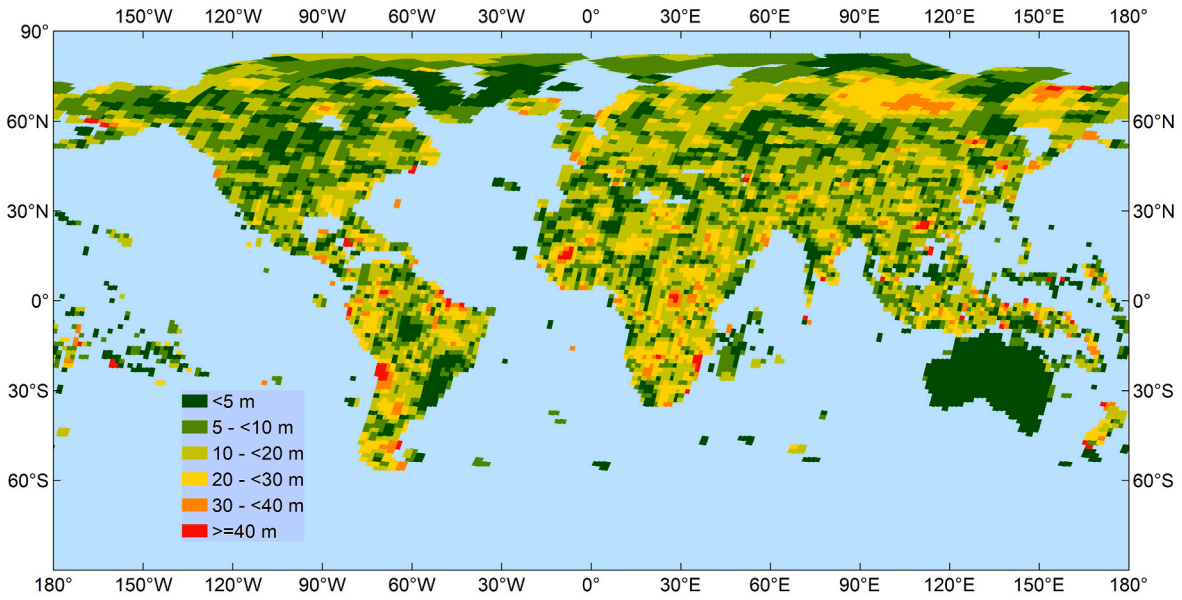

Fig. 1. Landsat WRS-2 path/row geolocation differences between the Collection 1 and Collection 2 Level 1 data products. The root-mean-square difference (RMSD) defined at each path/row are shown for Landsat 4–8.

Fig. 2. Illustration of Level 1 TP Landsat geolocation differences between Collection 1 and Collection 2 for a panchromatic (0.50–0.68 μm) 400 × 200 15 m pixel subset extracted from a Landsat 8 OLI image acquired over a path/row where the mean longitude and latitude geolocation collection shifts are large (25.64 m and 36.75 m respectively, 44.81 m RMSD). *Left*: Collection 2 15 m panchromatic band shown as red, green, blue. *Right:* Collection 1, Collection 2, Collection 2 panchromatic band shown as red, green, blue, respectively. The misregistration between the Collection 1 and Collection 2 images is apparent in the magenta and cyan tones in the right image. The Landsat 8 OLI image was acquired September 2, 2020, over WRS-2 path 125/row 43 and the subset is centered at 24.348°N, 109.361°E, near Liuzhou, China.

Northing directions and radially. In addition, all the processed Landsat Level 1 images are categorized into two tiers. L1TP images with radial RMSE ≤12 m are categorized as Tier 1, and as Tier 2 if they have radial RMSE >12 m. The L1GS and L1GT images are categorized as Tier 2 as no ground control is available to derive RMSE statistics and their geolocation is expected to be lower than for Tier 1. Users can refer to the RMSE L1TP image metadata and to the Tier categorization to ensure that they use appropriately geolocated imagery for their applications. Tier 1 images are more suitable for change detection and time series applications as the geolocation accuracy is less than half a 30 m pixel (Dwyer et al., 2018).

The improved geolocation provided by the Collection 2 processing is evident in Table 2, which summarizes the increased number of Tier 1 Level 1 images processed in Collection 1 compared to Collection 2. Considering all the tabulated sensors together, 11.95% more images were processed as Tier 1 in Collection 2. A minority of Landsat TM, ETM and OLI/TIRS images were categorized as Tier 1 in Collection 1 but were downgraded to Tier 2 in Collection 2. This occurred primarily because the image geolocation was more reliably characterized due to the greater number and quality of ground control used in Collection 2. Improvements to the ground control library included removal of early MSS era (1970s–1990s) ground control chips which reduced the number of Collection 2 MSS Tier 1 processed images by 1.16%. Landsat MSS geolocation is particularly challenging due to the lower quality and sometimes missing satellite ephemeris and attitude information, the coarser MSS spatial resolution compared to later sensor generations, and because of land cover change between the date of MSS image acquisition (1972–2012) and the up to decade(s) later ground control chip acquisition dates (Yan and Roy, 2021). Thus, as for Collection 1, less than 1% of the total MSS archive (not shown in Table 2) is processed to Tier 1 in Collection 2, whereas the proportion of the TM, ETM+, OLI/TIRS archive processed to Tier 1 increased from 62% in Collection 1–69% in Collection 2.

Table 2
Number of Collection 1 and Collection 2 Tier 1 Level 1 products available in the USGS Landsat archive acquired from July 23, 1972 to December 31, 2021. Numbers only include the daytime (descending orbit) Landsat image acquisitions.

Mission	Collection 1	Collection 2	Difference	Change
Landsat 1–5 MSS	11,682	11,546	−136	−1.16%
Landsat 4–5 TM	1,683,854	1,918,910	235,056	13.96%
Landsat 7 ETM+	2,154,133	2,390,190	236,057	10.96%
Landsat 8 OLI/TIRS	1,272,332	1,413,237	140,905	11.07%

3.2. Collection 2 improved sensor radiometric calibration

Landsat data are radiometrically calibrated to ensure that the reflected radiance imaged by the visible-to-shortwave infrared (VSWIR) spectral bands and the emitted radiance from the thermal infrared (TIR) spectral bands are consistent across the Landsat sensor record and reflect surface conditions rather than sensor artefacts. Prior to launch, all Landsat sensors are subject to laboratory measurements to characterize their radiometric and spectral responses and to quantify the relationship between the imaged radiance and the recorded digital numbers (DNs). In addition, the Landsat 8 OLI was subjected to a national laboratory traceable cross-calibration with the Sentinel-2 Multispectral Instrument (MSI) due to the similar MSI VSWIR spectral sampling and expected inter-use of OLI and MSI VSWIR imagery (Roy et al., 2014). Post-launch calibration is needed for Earth science missions because changes in the relationship between the imaged radiance and the recorded DNs can occur due to the stress of the satellite launch and/or sensor degradation over time. Consequently, all the Landsat sensors have, or had, some form of on-board lamps, solar diffusers, and blackbodies to provide on-orbit calibration data (Markham et al., 2004a, b, 2014). The resulting calibration information is often complemented by vicarious information obtained from a variety of sources including VSWIR observations of the moon (Markham et al., 2015) and of pseudo-invariant calibration sites (PICS) (Mishra et al., 2016) and TIR observations of deep space and water bodies characterized with *in situ* buoy thermal measurements (Hook et al., 2004; Barsi et al., 2014).

For Collections 1 and 2, the Landsat 8 OLI was used as the absolute VSWIR radiometric calibration reference and all previous Landsat sensors were cross calibrated to Landsat 8 using desert PICS targets (Micijevic et al., 2017). The TIR spectral bands were calibrated using thermal reference buoy measurements in coastal and inland water bodies (Schott et al., 2012; Barsi et al., 2014). The Collection 2 reprocessing enabled several radiometric improvements particularly for Landsat 5 and 8. The Landsat 8 TIRS absolute calibration was updated based on stray-light corrected vicarious calibration data (Schott et al., 2014). This resulted in a brightness temperature change from Collection 1 to Collection 2 of up to 0.2K and 0.6K for the Landsat 8 10.8 μm and 12.0 μm TIRS spectral bands over a 300K surface (Barsi et al., 2020). The Landsat 5 absolute calibration of the single TIR spectral band centered at 11.4 μm was updated for imagery acquired after January 1, 1997 to account for a residual bias error of 0.33K over a 300K surface (Micijevic et al., 2020). In addition, the Landsat 8 TIRS relative calibration was updated to account for variations in per-detector responsivities and reduced residual striping by 0.1–0.2% for most of the TIR detectors, with a minority changed by >1% (Barsi et al., 2020). The Landsat 8 OLI absolute calibration was updated for the shortest wavelength coastal aerosol (0.443 μm) and blue (0.482 μm) spectral bands to account for more complete knowledge of OLI responsivity degradation since launch and affected the data in these two spectral bands by up to 0.15% (Micijevic et al., 2020). The Landsat 8 OLI relative gains were also updated for all spectral bands to make use of actual responsivity measurement variations, rather than modeled future predictions. The resulting change was generally less than 0.2%, although some SWIR detectors may change by up to 2% (Micijevic et al., 2020). In addition, Landsat 8 OLI per detector bias estimates were modified to account for per-frame fluctuations reducing along-track striping and increasing the signal-to-noise ratio by 2–3% at typical radiances (Micijevic et al., 2019). The Collection 2 Landsat 8 reflectance calibration is well maintained with ~2% absolute reflective spectral band calibration uncertainty (Markham et al., 2014) and TIR spectral band uncertainties within 0.5 K in the 10.8 μm band and 0.75K in 12.0 μm band when expressed as a change in apparent temperature of a 300K surface (Barsi et al., 2020).

Landsat 9 data were first processed under Collection 2 using post-launch knowledge from the commissioning period. The Landsat 8 and 9 OLI and TIRS sensors are by design very similar but with some additional baffling added to the Landsat 9 TIRS telescope to reduce stray light contamination (Masek et al., 2020). After the September 2021 launch of Landsat 9, the commissioning phase included a cross-calibration with contemporaneous Landsat 8 imagery acquired by placing Landsat 9 into a slightly lower orbit with cross-calibration opportunities over a 6-day under-flight period (Gross et al., 2022; Kaita et al., 2022). Fig. 3 shows an under-flight example illustrating surface reflectance and surface temperature derived from contemporaneous Landsat 8 and under-flight Landsat 9 imagery over Baja California. The Landsat 9 OLI VSWIR bands were cross-calibrated to the corresponding Landsat 8 OLI spectral bands as the absolute calibration reference over a globally distributed set of sites during the 6-day period. The Landsat 9 TIRS spectral bands were calibrated to coastal and inland buoy data as described above.

The first sixteen months of Landsat 9 acquisitions (October 31, 2021 to February 28, 2023) were reprocessed using updated calibration parameters identified during this period. The calibration updates were needed to improve the relative gains between focal plan modules (banding) in the VSWIR bands, reduce detector swaps (striping) in the TIRS bands and TIRS absolute biases, and in addition, to improve TIRS to OLI sensor geometric alignment and the geometric accuracy of Landsat 9 L1GT processed imagery. Landsat 9 users can examine the processing date denoted in the filename or stored in the *DATE_PRODUCT_GENERATED* metadata and be cautious in their use of Landsat 9 processed before March 1, 2023 as they were processed without the updated calibration. The Collection 2 Landsat 9 OLI radiometric uncertainty is comparable or better than the Landsat 8 OLI (Micijevic et al., 2022) and TIRS spectral band uncertainties of approximately 0.65 K are evident when expressed as a change in apparent temperature of a 300K surface (Barsi et al., 2022).

While not a Collection 2 radiometric calibration improvement, users of Landsat 4 and 5 TM, and Landsat 7 ETM + data may occasionally find images with “caterpillar tracks” of anomalous pixel values (Helder et al., 2004; Storey and Choate, 2004). These pixel anomalies occur because the mechanical bumpers used to reverse the mirror scan direction in the TM and ETM + sensors degraded with age. This resulted in occasional stripes of isolated pixels with corrupted radiance values that can fall within the valid radiance range and so are difficult to detect using an automated technique. In Collection 2, for the first time, a new metadata parameter was added to denote the presence of these shutter intrusion events in effected images. In May 2003 the Landsat 7 ETM + scan line corrector (SLC) failed, removing pixel observations in stripes that increase in size towards the scan edge and reducing the useable amount of image data by about 22% (Markham et al., 2004a, b). A number of “SLC-off” gap filling algorithms have been proposed (Brooks et al., 2018; Yan and Roy 2020; Wang et al., 2020) but none have been implemented in Collection 2 as they are computationally expensive to implement and are imperfect.

3.3. Collection 2 level 2 surface reflectance

Landsat atmospheric correction of the reflective spectral bands has a long provenance. Early algorithms were based typically on dark-object subtraction that required users to identify dark objects in the image and assumed that the object TOA spectral reflectance was equal to the reflectance of the atmosphere that was then subtracted from all the image pixels (Chavez, 1996). Early algorithms did not correct for variations in the atmospheric scattering and absorbing constituents across the image, or account for multiple scattering (Ju et al., 2012). Modern algorithms use radiative transfer models in conjunction with atmospheric characterization data and image-based aerosol retrieval methods (Doxani et al., 2023). The Collection 2 Level 2 surface reflectance products are derived with global coverage for daytime images (solar zenith <76°) using algorithms based on the Second Simulation of a Satellite Signal in the Solar Spectrum Vector (6SV) radiative transfer code (Kotchenova et al., 2006). The Landsat 4–7 and the Landsat 8 and 9 TOA data are processed to surface reflectance using different 6SV

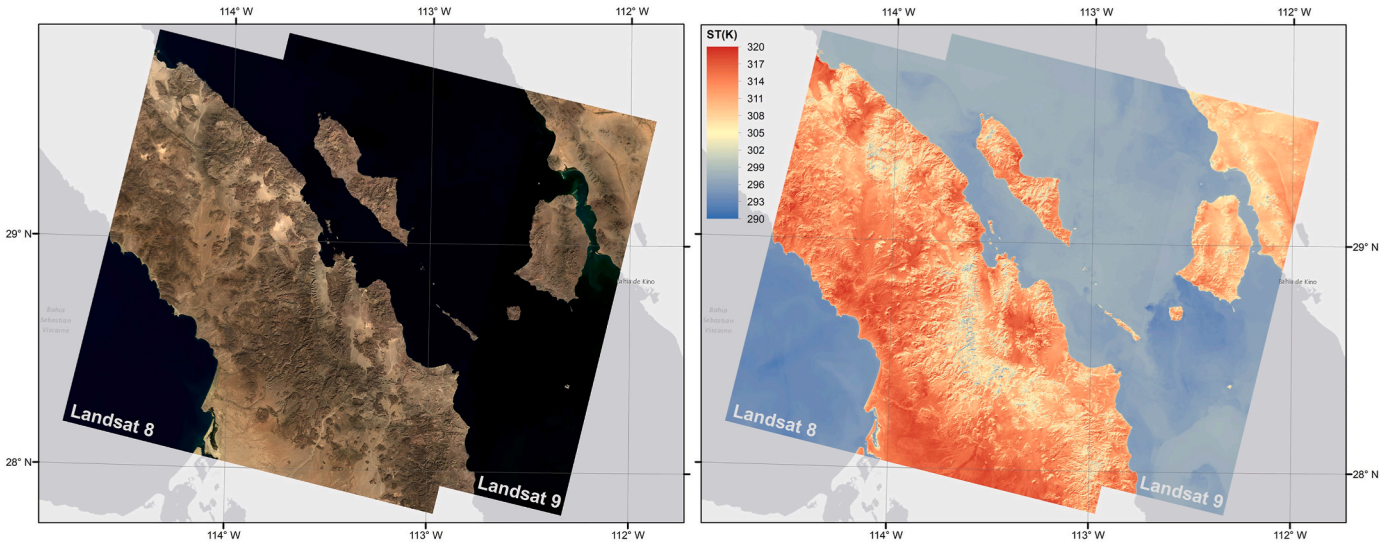

Fig. 3. Example of Landsat 8 and Landsat 9 under-fly data acquired November 15, 2021, over Baja California, Mexico (WRS-2 path 125/row 43) and processed with Collection 2 algorithms. *Left:* Level 2 surface reflectance (true color red/green/blue surface reflectance scaled with the same stretch in each band from $\rho = 0.0$ to 0.4), *Right:* Level 2 surface temperature.

implementations that are described below. The Landsat 1–5 MSS data are not atmospherically corrected in Collection 2 because the MSS has no blue or SWIR bands and there were sparse auxiliary atmospheric characterization data in the MSS Landsat 1–3 era.

The Landsat 4–7 data are atmospherically corrected using the Landsat Ecosystem Data Adaptive Processing System (LEDAPS) algorithm (Masek et al., 2006). The LEDAPS algorithm uses a per-band 6SV parameterized Look up Table (LUT) for a range of aerosol values, elevation data (i.e., for surface pressure derivation), and near contemporaneous auxiliary ozone, water vapor obtained from a variety of sources (Table 3). The aerosol optical thickness (AOT) is retrieved independently using a dense dark vegetation (DDV) approach. The Landsat 4–7 Level 2 surface reflectance for each VSWIR band is provided with per-pixel atmospheric opacity information and Quality Assessment (QA) flags defining the DDV pixels, and other pixel conditions used in the LEDAPS processing. The surface reflectance atmospheric opacity and the LEDAPS cloud QA bands present in Landsat 4–7 Collection 2 surface reflectance product are defined in Table 4.

Table 3
Atmospheric auxiliary data ingest for Landsat Collection 2 Level 2 product generation. Abbreviations: LaSRC (Land Surface Reflectance Code), LEDAPS (Landsat Ecosystem Disturbance Adaptive Processing System), 6SV (Second Simulation of a Satellite Signal in the Solar Spectrum), MODIS (Moderate Resolution Imaging Spectroradiometer), CMG (Climate Modelling Grid), VIIRS (Visible Infrared Imaging Radiometer Suite), MISR (Multi-angle Imaging SpectroRadiometer), NOAA (National Oceanic and Atmospheric Administration), ETOPO5 (Earth Topography Five Minute Grid), TOMS (Total Ozone Mapping Spectrometer), OMI (Ozone Monitoring Instrument), NCEP (National Centers for Environmental Prediction), MODTRAN (MODerate resolution atmospheric TRANsmission), MERRA-2 (Modern-Era Retrospective analysis for Research and Application Version 2), GEOS (Goddard Earth Observing System), Forward Processing for Instrument Teams (FP-IT), Instrument Teams (IT), ASTER (Advanced Spaceborne Thermal Emission and Reflection Radiometer), GED (Global Emissivity Dataset), GLS (Global Land Survey), NASADEM (NASA Shuttle Radar Topography Mission), CDEM (Canadian Digital Elevation Model), SNF (Sweden, Norway, and Finland National Elevation Data), NED (National Elevation Dataset for Alaska), GIMP (Greenland Ice Mapping Project), NPI (Norwegian Polar Institute).

Level 2 Product	Algorithm	USGS Algorithm Ver.	Radiative Transfer Model/Program	Auxiliary data	Description	Horizontal Resolution	Latency
Surface Reflectance	LaSRC	1.5.0	6SV (refined to take advantage of added CA band)	MODIS C6 CMG (2013–2/16/2023)	Coarse-resolution ozone and water vapor	0.05°	2 days
				MODIS C6.1 CMG (2/17/2023-present); transition to VIIRS C2 CMG is underway.			
				MODIS/MISR derived ratio maps	To capture seasonal/annual variability in the ratio between red and blue channels for AOT retrieval	0.05°	Static
	LEDAPS	3.4.0	6SV	NOAA ETOPO5 DEM	To derive surface air pressure	5 arcmin	Static
				TOMS (1978–2004), OMI (2004-present)	Ozone	1.25 × 1 deg	3 days
				NCEP grid	Water vapor, atmospheric pressure, air temperature	2.5 × 2.5 deg	4 days
Surface Temperature	Single Channel	1.3.0	MODTRAN	NOAA ETOPO5 DEM	Digital elevation model	5 arcmin	Static
				MERRA-2 (1982–12/31/1999), GEOS FP-IT (01/01/2000-present); transition to GEOS IT is underway.	Atmosphere profiles of geopotential height, specific humidity, and air temperature	0.625 × 0.5 deg	18 h
				ASTER GED	Surface emissivity	100 m	Static
				GLS DEM, NASADEM, CDEM, SNF, Alaska NED, GIMP, NPI, ArcticDEM	Regional digital elevation model	3 arcsec	Static

Table 4
Landsat Collection 2 Level 1 and Level 2 per-pixel quality assessment (QA) information.

QA Band	Description
Landsat 4–9 Pixel Quality Assessment (QA_PIXEL)	Derived from the Function of Mask (FMask) version 3.3.1, the bit-packed Pixel QA defines certain quality conditions such as cloud, cloud shadow, and snow/ice flags with associated confidence levels. The cirrus and cirrus confidence levels in Landsat 8–9 QA_PIXEL are determined using a separate cirrus detection algorithm. A water flag is also included to support advanced level science products. The high-confidence cloud pixels are dilated (3-pixels) and flagged as such in this QA band.
Landsat 4–9 Radiometric Saturation QA (QA_RADSAT)	Represents which sensor bands were saturated during data capture, yielding unusable data. Saturation is not common in Landsat 8/9. Saturation occurs over the reflective surfaces in the Visible and Near Infrared (VNIR) bands, or volcanoes and wildfires in the Shortwave Infrared (SWIR) and thermal bands.
Landsat 8/9 Aerosol QA (SR_QA_AEROSOL)	An internal Landsat 8/9 Land Surface Reflectance Code (LaSRC) QA band that provide low-level details about the validity of the aerosol retrieval. It also shows whether a terrestrial or water-based routine was used for aerosol determination. The Aerosol QA also indicates if the aerosol was inverted or interpolated from the center of 3 × 3 windows.
Landsat 4–7 LEDAPS SR Cloud QA (SR_CLOUD_QA)	An internal Landsat Ecosystem Disturbance Adaptive Processing System (LEDAPS) QA band that flags the Dark Dense Vegetation (DDV) pixels used in Aerosol Optical Thickness (AOT) calculation. The LEDAPS SR cloud QA also provides per-pixel information about the cloud, cloud shadow, snow, and water conditions. Although these conditions are defined in the QA_PIXEL, the LEDAPS algorithm executes its own calculations to meet the specific requirements of the atmospheric correction routines.
Landsat 4–7 SR Atmospheric Opacity (SR_ATMOSOPACITY)	Provides a generalized measure of the atmospheric opacity generated by the Landsat Ecosystem Disturbance Adaptive Processing System (LEDAPS) algorithm and based on the radiance viewed over the Dark Dense Vegetation (DDV) pixels within the scene. Values less than 0.1 are clear, 0.1–0.3 are average, and values greater than 0.3 indicate haze or other cloud conditions. The SR values from pixels with high atmospheric opacity are less reliable, especially under high Solar Zenith Angle (SZA) conditions.
Landsat 4–9 ST Uncertainty (ST_QA)	Provides the per-pixel ST product uncertainty (K). The uncertainty propagation model includes the uncertainty in atmospheric variables, Landsat radiance uncertainty, the error associated with the Advanced Spaceborne Thermal Emission and Reflection Radiometer (ASTER) Global Emissivity Dataset (GED) emissivity, and uncertainties in the distance to cloud and transmission.

The Landsat 8 and 9 data are atmospherically corrected using the Land Surface Reflectance Code (LaSRC) (Vermote et al., 2016). The LaSRC algorithm uses a 6SV parameterized Look up Table (LUT) of discrete AOT values and also water vapor and ozone derived from near contemporaneous MODIS Climate Modelling Grid (CMG) data (Table 3). In the LaSRC algorithm, the AOT is inverted using spectral ratios of the OLI coastal aerosol, blue, and red spectral bands. Over water, a red spectral band AOT LUT is used. In Collection 2, the LaSRC code was modified to make the code run more efficiently and to ensure processing traceability where every pixel is consistently processed to Level 2 surface reflectance. The AOT is retrieved with respect to 3 × 3 30 m pixel windows instead of the original per-pixel retrieval implementation. In addition, a semi-analytical approach is used to estimate the atmospheric transmission, intrinsic reflectance, and spherical albedo more efficiently based on a cubic polynomial fit of the AOT LUT values. The AOT at the center of the 3 × 3 30-m pixel window is optimized by iteratively calling the atmospheric correction function until the AOT inversion converges. Window locations where the AOT retrieval fails are flagged, and their AOT values are gap-filled from surrounding windows. An inverse distance weighted interpolation is then applied to obtain AOT estimates for every 30-m pixel. The Landsat 8 and 9 Level 2 surface reflectance is computed for each VSWIR spectral band and is provided with similar per-pixel QA flags as for the LEDAPS (Landsat 4–7) surface reflectance. Additional surface reflectance aerosol QA flags are included that document the validity of the aerosol retrieval, whether a land or water-based algorithm was used for the aerosol inversion, or if the aerosol was interpolated from surrounding pixels are included (Table 4).

The Collection 2 Level 2 Surface Reflectance is produced globally and in general performs as expected (Fig. 3). As usual, a minority of atmospherically corrected pixels may have values outside their theoretical limits, i.e., reflectance >1.0 or <0.0 (on the unitless reflectance scale) due to "overcorrection" associated primarily with incorrect atmospheric characterization (Roy et al., 2014) and over surfaces that reflect light in the satellite observation direction more strongly than a Lambertian surface (Schaepman-Strub et al., 2006). A known Collection 2 issue for the Landsat 8 and 9 Level 2 surface reflectance products occurs over snow and ice where the AOT inversion can fail and the AOT interpolated from neighboring values is insufficiently representative, causing reflectance >1.0, particularly in the shorter wavelength spectral bands. Users are encouraged to examine the per-pixel Aerosol QA information, especially the validity of aerosol retrieval (bit 1) and the qualitative aerosol level (bits 6 and 7). Pixels with invalid retrieval and high aerosol levels indicate greater uncertainty in surface reflectance and can be used to mask reflectance values > 1. For example, the top row of Fig. 4 shows Level 2 surface reflectance over and around Lake Tahoe acquired by the Landsat 8 OLI in the Spring (left column) and Summer (right column), and the middle and bottom rows show the per-pixel QA information. In the Spring there are many invalid AOT pixels (red tones) present over the snow-covered terrain in the south and west which indicate uncertain surface reflectance values. Conversely, in the Summer most of the terrestrial pixels have valid AOT retrievals.

The LEDAPS and LaSRC source algorithms have been systematically evaluated against AErosol RObotic NETwork (AERONET) measurements (Vermote et al., 2016; Ju et al., 2012; Roger et al., 2022), MODIS Collection 5 surface reflectance products (Feng et al., 2013), and ground-based *in situ* reflectance (Maiersperger et al., 2013; Nazeer et al., 2014; Vuolo et al., 2015). Recent community exercises including the Atmospheric Correction Intercomparison eXercise (ACIX) provide a forum for surface reflectance validation (Doxani et al., 2023). Validation of the USGS-generated Collection 2 Level 2 surface reflectance products is underway and will include the use of data collected by new imaging systems mounted on stationary towers to measure heterogeneous vegetated sites (Vermote et al., 2022) and will enable meaningful validation of atmospheric corrections to account for surface heterogeneity i.e., adjacency effects (Ouaidrari and Vermote, 1999; Liang et al., 2001).

Older Landsat sensor generations were not designed for water monitoring. The OLI on Landsat 8 and 9 has sufficiently high radiometric resolution and spectral characteristics to enable water quality and aquatic information retrieval (Pahlevan et al., 2017). However, the LaSRC atmospheric correction was not designed to compute reflectance over water, and users should be cautious in using the Collection 2 Level 2 surface reflectance product for water and aquatic science applications.

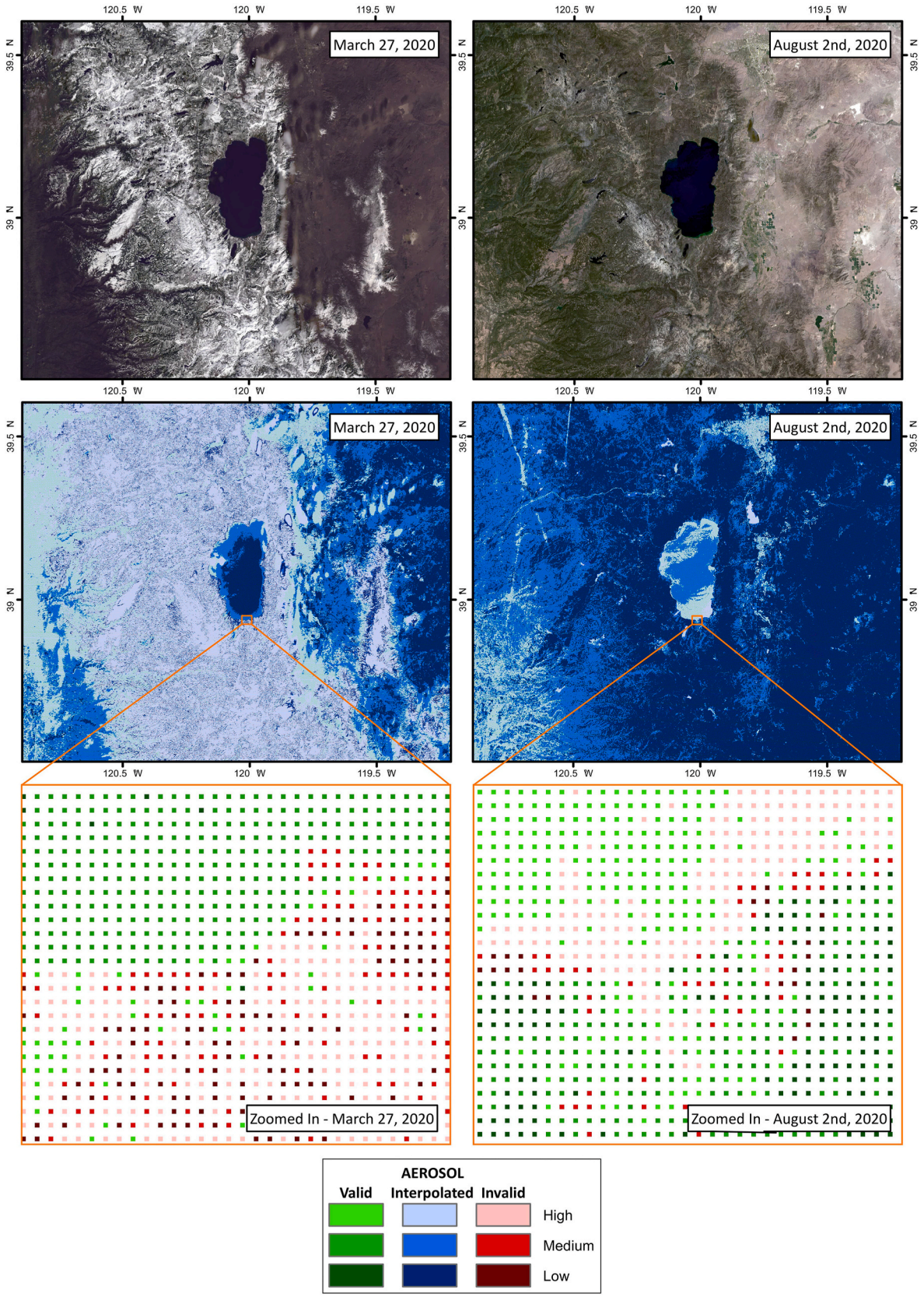

Fig. 4. Collection 2 Level 2 surface reflectance from Landsat 8 acquired over Lake Tahoe, California region (WRS-2 path42/row33) in the Spring March 27; (*left*) and Summer August 2; (*right*) of 2020. *Top row*: surface reflectance (true color red/green/blue surface reflectance scaled linearly between $\rho = 0.0$ to 0.4 reflectance units); *Middle row*: per-pixel Aerosol QA information; *Bottom row*: a 2.4 × 2.8 km spatial subset of the per-pixel Aerosol QA information showing for illustrative clarity the QA information for every third 30-m pixel in the x and y image directions.

Instead, the USGS EROS Center is currently offering an on-demand provisional Collection 2 Level 2 aquatic reflectance product through the EROS Science Processing Architecture On Demand Interface (ESPA) (https://espa.cr.usgs.gov).

3.4. Collection 2 level 2 surface temperature

Surface skin temperature varies rapidly in space and time as a function of several environmental factors. Reliable temperature derivation from satellite thermal infrared (TIR) radiance requires correction for atmospheric absorption and temperature effects, and knowledge, or retrieval, of the spectral surface emissivity. The Landsat 4 and 5 TM had one 120-m TIR band centered at around 11.4 μm, the Landsat 7 ETM + had a 60-m TIR band centered around 11.4 μm with low and high gain settings, and the Landsat 8 and 9 Thermal Infrared Sensor (TIRS) has two 100-m bands centered at 10.8 μm and 12.0 μm. There were no TIR spectral bands on the earlier Landsat 1–2 missions, and the Landsat 3 TIR spectral band failed shortly after launch (Goward et al., 2017). In principle, two TIRS bands enable improved surface temperature estimation using a split window algorithm to reduce differential atmospheric absorption (Wan and Dozier, 1996; Reuter et al., 2015). Unfortunately, the two Landsat 8 TIRS bands, and in particular the 12.0 μm band, were found post-launch to have stray light issues (Montanaro et al., 2014). The Landsat 8 TIRS stray light was compensated for using an optical stray light model and the observations at the swath edges (Gerace and Montanaro, 2017) and the corrected TIRS data were shown to be able to provide split window surface temperature retrievals with a 0.2 K mean error (Gerace et al., 2020). However, due to schedule issues, the Collection 2 Level 2 surface temperature products are derived using only a single channel algorithm applied to the 11.4 μm radiance (Landsat 4–7) and to the 10.8 μm radiance (Landsat 8–9). The Landsat 7 ETM + surface temperature is derived using both the low and a high gain 11.4 μm radiance to provide a single pixel retrieval that saturates less frequently.

The Collection 2 Level 2 Surface Temperature product is derived with global coverage for daytime images (solar zenith $<76°$) for Landsat 4–9. The surface temperature (units: Kelvin) is provided on a 30 m grid consistent with the shortwave datasets (although the nominal resolution of the TIR data is coarser, 60–120 m), and is accompanied by per-pixel uncertainty (units: Kelvin) of surface temperature measurement to enable downstream analysis of retrieval quality (Table 4). In addition, atmospheric transmittance, upwelled path radiance, and downwelled sky radiance information is provided to facilitate product generation traceability. The Collection 2 surface temperature algorithm is based on the MODerate resolution atmospheric TRANmission (MODTRAN) radiative transfer code (Malakar et al., 2018). The MODTRAN algorithm uses contemporaneous atmospheric auxiliary information (Table 3) including profiles of the air temperature, geopotential height, and specific humidity information that are extracted (depending on the image acquisition date) either from Modern-Era Retrospective analysis for Research and Application, Version 2 (MERRA-2) (Gelaro et al., 2017) or Goddard Earth Observing System-5 (GEOS-5) Forward Processing for Instrument Teams (FP-IT) (Lucchesi, 2017) reanalysis data. The surface spectral emissivity that is needed to derive surface temperature cannot be retrieved from a single TIR band. Instead, spectral emissivity at 11.3 μm (for Landsat 4–7) and 10.7 μm (for Landsat 8–9) obtained from the Advanced Spaceborne Thermal Emission and Reflection Radiometer (ASTER) Global Emissivity Database (GEDv3) are used. The GEDv3 provides a near global coverage of spectral emissivity values and was generated by applying the Temperature Emissivity Separation (TES) algorithm to the five 90-m ASTER TIR bands and averaging over the cloud-free observations from 2000 to 2008 (Hulley et al., 2015; Malakar et al., 2018). The mean spectral emissivity associated with Landsat TIR spectral bands is estimated by applying sensor-specific regression coefficients on ASTER 10.7 and 11.3 μm bands. Since the ASTER GEDv3 is static, the spectral mean emissivity from ASTER era is adjusted for Landsat overpass conditions to account for vegetation and snow cover changes (Hulley et al., 2015; Malakar et al., 2018).

The single channel algorithm used to generate the Collection 2 Landsat surface temperature product has been validated using select Landsat 5 and 7 data over land sites and inland and coastal water with an accuracy of within 0.51 K and precision of 1.56 K (Cook et al., 2014; Laraby and Schott, 2018; Gerace et al., 2015; Malakar et al., 2018). The Collection 2 Landsat 8 surface temperature product has been validated over a variety of land sites with ~0.5 K accuracy and ~1K precision, and over lake and coastal water sites with approximately 50% better performance (Fig. 5). The land sites have lower accuracy and precision due to the larger variability in surface emissivity compared to water bodies. There is an outstanding need for comprehensive validation of the Collection 2 surface temperature products across a range of geographic regions and land surface types and for Landsat 4–9.

3.5. Cloud and cloud shadow mask

Clouds and their shadows preclude reliable surface monitoring. Like Collection 1, the 30 m cloud and shadow masks are included in the Collection 2 Level 1 and 2 products. The Landsat Collection 2 per-pixel QA includes information on cloud, cloud shadow, cirrus, snow/ice, and water presence. This QA layer also provides low, medium, and high-confidence levels for cloud, as well as low and high-confidence levels for shadow, snow/ice, and cirrus presence (Table 4).

The Landsat cloud detection has a heritage based on the application of empirical spectral tests to single image pixels (Irish et al., 2006; Zhu and Woodcock, 2012; Foga et al., 2017; Skakun et al., 2019). The Collection 2 cloud and cloud shadow masking algorithm uses the USGS Landsat Collection 1 C Function of Mask (CFMask) algorithm version 3.3.1 (Foga et al., 2017) developed by Zhu et al. (2015). The CFMask algorithm was validated as having an overall accuracy of 90.45%, although comprehensive validation of cloud mask products is challenging given the considerable variability in the optical properties and morphology of clouds. In particular, cloud detection over snow and ice, and shadow detection over low reflectance surfaces, can be challenging due to spectral similarity. The inclusion of a 1.360–1.390 μm spectral band on the Landsat 8 and 9 OLI enabled cirrus cloud detection with low and high confidence, which is needed given the pervasiveness of cirrus in Landsat imagery (Kovalskyy and Roy, 2015). The OLI cirrus cloud detection is undertaken by thresholding the OLI 1.360–1.390 μm TOA reflectance with a non-linear adjustment for column water vapor effects based on the surface elevation defined using the Landsat geolocation DEM (Section 3.1). Future cirrus detection improvements may be necessary as the cirrus detection algorithm can misclassify pixels in dry atmospheric conditions and over snow/ice surfaces that reflect strongly in the 1.360–1.390 μm region (Qiu et al., 2020).

3.6. Level 1 and level 2 product format

The Collection 2 Level 1 and 2 products are provided as ~185 km × 180 km images in the UTM projection (or PS projection for Antarctic scenes with center latitude $\geq 63°$S). The images are defined in the WRS path and row coordinate system. The first three Landsat satellites were in a higher orbit (917 km) with a greater repeat (18-days) compared to the later satellites (705 km orbit, 16 day repeat) (Goward et al., 2017). Consequently, the Landsat 1, 2 and 3 products are defined using the WRS-1 path and row coordinate system, while the Landsat 4–9 products are defined using the WRS-2 system to account for swath coverage differences. Periodic station-keeping maneuvers (i.e., inclination burns) are implemented to maintain the Landsat satellite ground track and orbit phase. Notably, Landsat 5 experienced significant orbit drift particularly when it was operated commercially from 1985 to 2001 (Zhang and Roy, 2016). The Landsat 7 orbit was allowed to drift after the final station-keeping maneuver in 2017 with increasing changes during its extended science mission between 2022 and 2023. For all the Landsat

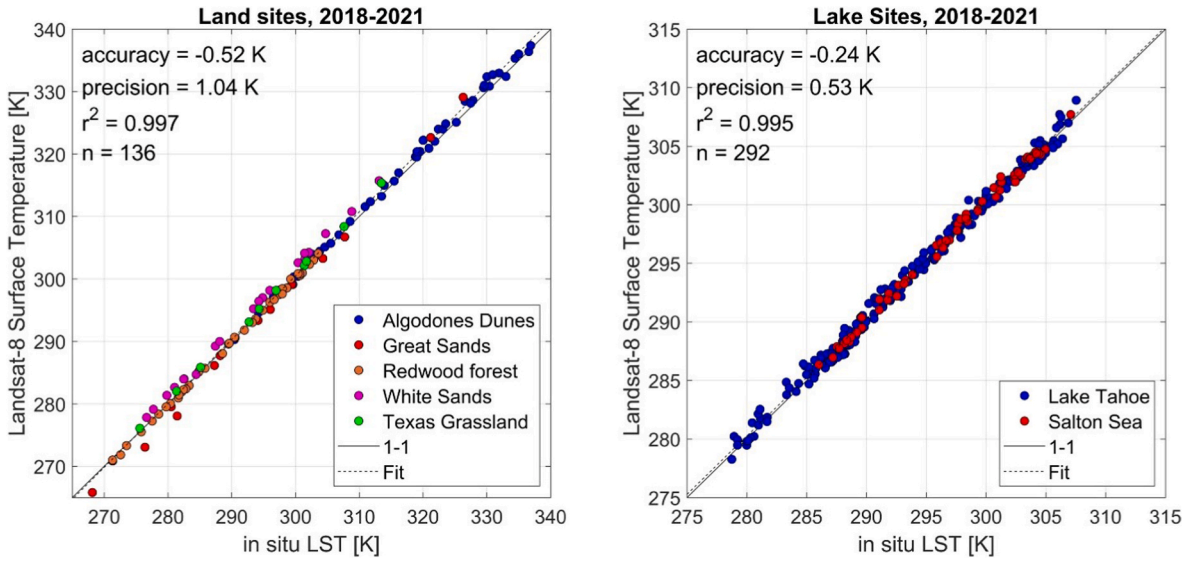

Fig. 5. Example validation of the Collection 2 Landsat 8 surface temperature products for land sites (left) and lake sites (right) derived from hundreds of cloud-free acquisitions acquired 2018–2021.

missions, orbit perturbations mean that the ground locations (latitude and longitude) of the Leve1 1 and Level 2 product pixel locations occurring in the same WRS path/row typically change between overpasses. For example, drifts of several kilometers east-west and less than a kilometer north-south were found from global analysis of three years of global Landsat 5 TM and Landsat 7 ETM + imagery (Kovalskyy and Roy, 2013). Consequently, Level 1 or 2 products acquired over the same WRS path/row need to be aligned prior to temporal analyses.

The Collection 2 Level 1 and 2 products store each pixel and spectral band as 16-bit unsigned integer digital numbers (DNs). The DNs may be converted to physical units, i.e., TOA spectral radiance (Level 1) or TOA reflectance, surface reflectance, TOA brightness temperature, and surface temperature (Level 2) using band specific scale factors and offset values stored in the product metadata. The Level 1 TOA radiance and TOA reflectance are stored assuming a solar zenith angle = 0° and can be corrected using the solar zenith angle at the time of acquisition. The solar zenith angle (SZA), solar azimuth angle (SAA), view zenith angle (VZA), and view azimuth angle (VAA) are provided for each 30 m pixel for Landsat 4–9 in the Collection 2 Level 1 product. These angles are not available for Landsat 1–3 because of uncertainties in the Landsat MSS line-of-sight calculation due to sometimes sparse and less-precise satellite ephemeris information.

The Collection 2 Level 1 products include per-pixel QA bands that document the cloud detection confidence, cloud shadows, water, and snow/ice detection confidence, radiometric saturation, and terrain occlusion (Table 4). The Collection 2 Level 1 QA bands were revised from Collection 1 to facilitate consistency between Level 1 and Level 2 processing, and to accommodate the expanded per-pixel Level 2 QA bits included within Level 2 surface reflectance and surface temperature products.

3.7. Collection 2 U.S. Analysis ready data

Landsat U.S. ARD are generated for the Landsat 4–9 30 m record over the conterminous United States (CONUS), Alaska, and Hawaii. The Landsat ARD were developed to provide easy-to-use data, to enable analysis with a minimum of additional effort, and support the downstream development of higher-level products (Dwyer et al., 2018). The ARD store 30 m (i) surface reflectance, and (ii) top of atmosphere (TOA) reflectance, for each of the VSWIR spectral bands, (iii) TOA brightness temperature for the TIR band(s), (iv) the surface temperature, and (v) associated per-pixel quality assessment information. Both TOA and surface estimates are stored as certain users prefer TOA data, particularly over snow and water where atmospheric correction can be less reliable (Fahnestock et al., 2016; Scambos et al., 2018; Zhai et al., 2022), and to facilitate the development of next generation atmospheric correction and temperature retrieval algorithms.

The Landsat ARD are generated by application of the Collection 2 Level 1 and 2 processing algorithms to the Level 0 data and then reprojecting the results into fixed non-overlapping tiles defined in the Albers equal area projection. Notably the Landsat data are not resampled twice but rather are projected directly to the Albers projection to reduce resampling degradations (Shlien, 1979; Li et al., 2017). To ensure that the ARD are geometrically consistent through time, only Landsat images that can be aligned with image-to-image tolerances of ≤12 m radial root mean square error (Tier 1 data) are used in the ARD processing (Dwyer et al., 2018). Consequently, the Landsat ARD does not include Landsat MSS data as the majority of MSS acquisitions cannot be geolocated to this accuracy (Yan and Roy, 2021). Given the high geolocation accuracy of more recent Landsat sensors (Storey et al., 2019), all Landsat 8 and 9 images are processed to the U.S. ARD. Notably, because the geographic coordinates of each ARD tile pixel are fixed, no additional processing and alignment steps are necessary prior to multi-temporal analysis. This is in contrast, as noted in Section 3.6, to the Level 1 and 2 products defined in the UTM and PS projections. Further, unlike for the Level 1 and 2 products, the ARD are defined in an equal area projection which is convenient for summarizing the areas of terrestrial attributes and for large area analyses (Dwyer et al., 2018). Indeed, the Albers projection is the same as that used by other CONUS-wide remote sensing products including the USGS National Land Cover Database (NLCD) (Wickham et al., 2021), the United States Department of Agriculture (USDA) National Agricultural Statistics Service (NASS) Cropland Data Layer (CDL) (Johnson and Mueller, 2010), and the USGS Land Change Monitoring, Assessment, and Projection (LCMAP) product (Brown et al., 2020).

The Landsat ARD are provided in fixed and non-overlapping 5000 × 5000 30-m pixel (150 × 150 km) tiles referenced by horizontal (h) and vertical (v) tile coordinates. Each individual orbit of Landsat data overlapping an U.S. ARD tile is stored independently. The tiling scheme is based on an original one developed by an early NASA-funded Landsat ARD project (Roy et al., 2010). Fig. 6 illustrates Landsat 8 (left column) and Landsat 9 (right column) OLI 30 m surface reflectance (top row) and surface temperature (bottom row) for a 15 × 15 km spatial subset of a single ARD tile in California. The Landsat 8 and 9 imagery sensed over

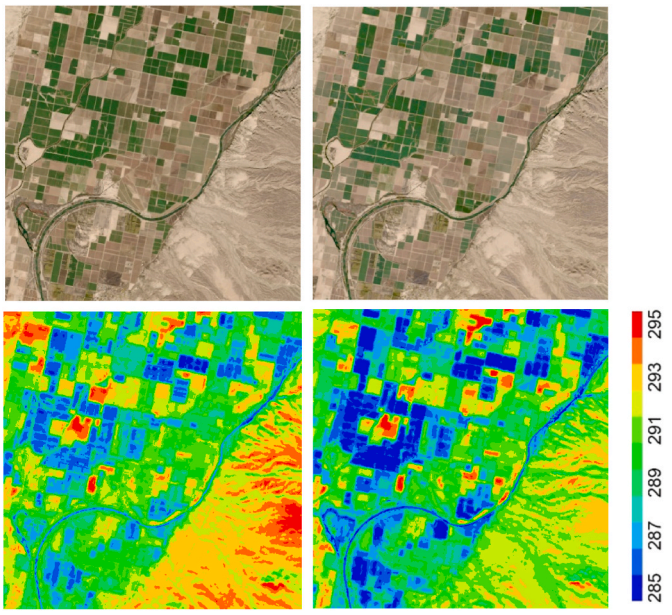

Fig. 6. Collection 2 Landsat ARD example over an agricultural region in California (15 × 15 km spatial subset from CONUS ARD tile h05v13, centered on 33.442°N 114.659°W). *Left column*: Landsat 8 data sensed December 15, 2021, *Right column*: Landsat 9 data sensed December 16, 2021. *Top row:* true color surface reflectance (red, green, blue spectral bands). *Bottom row*: surface temperature (K).

the tile area were acquired on December 15th and 16th 2021, respectively, and in this one day period the surface reflectance did not change significantly but the temperature changed by > 6 K at certain 30-m ARD pixel locations. The Landsat ARD were first made available in Collection 1, and the ARD geographic coverage was extended in Collection 2 in response to user requests, particularly over the Aleutian Islands, the Great Lakes, and some other coastal regions (Fig. 7). In addition, the ARD tiles were expanded by including WRS-2 path/rows that intersected within a 15-km coastal buffer zone around the U.S. shoreline and the Great Lakes. This resulted in a total of 81, 2 and 73 ARD tiles being added or updated in Collection 2 over the CONUS, Hawaii and Alaska, respectively.

4. Landsat collection 2 access and latency

The Landsat Collection 2 products are available in the standard way from the legacy USGS Earth Explorer (https://earthexplorer.usgs.gov) portal and also for bulk ordering via the USGS/EROS machine-to-machine (M2M) application programming interface (API). Notably, the Collection 2 products can also be accessed directly from the commercial cloud through the USGS's Cloud Hosting Solutions (CHS) US West-2 AWS Simple Storage Service (S3) bucket (https://registry.opendata.aws/usgs-landsat/). This AWS storage enables users to bring their applications to the Landsat archive rather than needing to download Landsat data to their local computer. The USGS pays for the Landsat Collection 2 AWS storage costs. However, users processing Landsat data directly in AWS will need to pay for their AWS processing costs, any temporal file storage in AWS, and for egress of derived products.

Landsat was not designed for near-real time applications because of the low revisit interval (nominally 16-days for Landsats 4–9 and 18-days for Landsats 1–3). Consequently, efforts to minimize the latency between image acquisition and the availability of the processed data were not a priority compared to other processing considerations. However, in Collection 2 aspects of the processing were reengineered to reduce the latency for newly acquired Landsat 8 and 9 data (Table 5). Recall that the Collection 2 Landsat 8 and 9 data are generated on-premises at USGS EROS and a rolling cache of the previous 90 days of processed acquisitions are retained to facilitate bulk data access. The USGS makes Landsat 8 OLI and TIRS products available shortly after acquisition to support a nascent NRT product demand even though TIRS geolocational uncertainty is higher until additional geometric processing is conducted for the Tiered Level 1 and Level 2 processing. The Landsat 9 latency is much improved over Landsat 8 with the ability to generate a Level 1 product

Table 5
Latency between acquisition and availability of Collection 2 Landsat 8 and 9 products.

	LEVEL 1 REAL TIME (RT)	LEVEL 1 TIERED	LEVEL 2 TIERED
LANDSAT 9 OLI/TIRS	Not Applicable	4–6 h	2–3 days
LANDSAT 8 OLI/TIRS	4–6 h	3–10 days	4–11 days

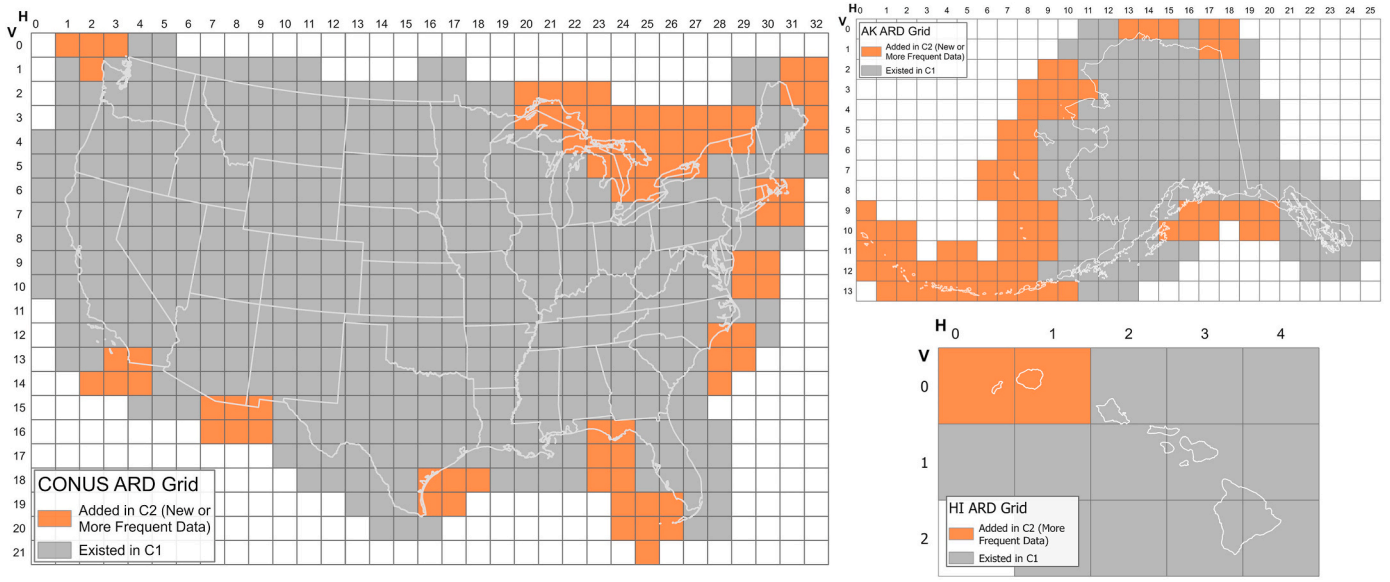

Fig. 7. Landsat Collection 2 ARD horizontal (h) and vertical (v) tile coordinates for CONUS, Alaska, and Hawaii. The grey and orange shades highlight Collection 1 and Collection 2 differences where either a new ARD tile was added or more WRS-2 path/row data were included.

within four to 6 h after acquisition because TIRS on Landsat 9 does not require additional Scene Select Mechanism (SSM) processing like Landsat 8. The Landsat Collection 2 Level 2 scene-based and the U.S. ARD are on average, generated within 24 h of the Tiered Level 1 products being processed.

All data released by the USGS on servers owned by, or managed under contract to, the USGS, are assigned a Digital Object Identifier (DOI). A DOI is a string of numbers, letters and symbols used to uniquely identify a dataset and to provide it with a permanent internet accessible address. The DOI remains fixed over the dataset lifetime, whereas a website location may change. Table 6 summarizes the availability and DOIs used to identify the Collection 2 archive.

5. Discussion and future collection plans

Collection 2 is an important step towards improving the consistency of the Landsat record. This is challenging given the significant technological changes and the availability of ancillary data that have occurred since the launch of Landsat 1 in 1972. The Landsat Collection 2 products have two core improvements over Landsat Collection 1. First, the absolute geolocation accuracy was improved by exploiting the availability of ESA Sentinel-2 GRI data and the on-orbit geometric performance of Landsat 8. Second, Level 2 atmospherically corrected surface reflectance and surface temperature products are now available for the global 30 m Landsat 4–9 record and are generated operationally as new Landsat 8 and 9 observations are acquired. While these changes reflect major product achievements, there are several existing Collection 2 product improvements that have been identified for when the time comes to reprocess the consolidated Landsat global data archive for a third time as Collection 3. They are described below and discussed in the context of the lessons learned from Landsat Collection 1 and Collection 2.

The USGS was able to improve the Landsat geolocation accuracy because of the Landsat 8 OLI on-orbit geometric performance, which is currently matched or exceeded by the Landsat 9 OLI (Masek et al., 2020), and the availability of ESA GRI data that together were used to update the Landsat ground control library used in Collection 2. The international cooperation between USGS, NASA, and ESA, resulted in more accurate geolocation than previously observed for the Landsat mission data and importantly supports the reliable harmonization of Landsat 8/9 data with ESA Sentinel-2A/B data (Storey et al., 2016). The number of Landsat Tier 1 Level 1 products (i.e., geolocated with a radial RMSE <12 m) increased by $>10\%$ from Collection 1 to Collection 2 for all the Landsat sensor generations except for MSS (Table 2). Fig. 8 shows by sensor the geographic distribution of the Tier 1 changes. For all sensors, snow-prone high latitude and certain desert regions had greater numbers of acquisitions downgraded from Tier 1 to Tier 2 than elsewhere. This occurred primarily because the image geolocation was more reliably characterized due to the greater number and quality of ground control used in Collection 2. The greater number and spatial coverage of the later Landsat mission acquisitions (Wulder et al., 2016) is also evident. Future research to consider the impacts of changing the radial RMSE 12 m threshold value in future collection processing for a more refined Tiering categorization is recommended. As for Collection 1, less than one percent of the total MSS archive was processed as Tier 1 in Collection 2 for the reasons discussed in detail in Section 3.1. For Collection 3, improvement of the MSS geolocation accuracy is needed to increase the number of MSS images that can be processed to Tier 1 accuracy to support time series applications, and to enable the MSS data to be included in the U.S. Landsat ARD data suite.

The Landsat Level 2 surface reflectance product has a long development heritage (from MODIS and AVHRR) and is quite mature. However, a known Collection 2 issue for the Landsat 8 and 9 surface reflectance product over snow and ice (described in Section 3.3) is pending resolution. The Landsat surface reflectance product requires a variety of auxiliary atmospheric characterization data that cannot be retrieved from Landsat observations alone (Table 3). In particular, auxiliary atmospheric characterization data were unavailable in the 1970s and 1980s and seasonally dependent climatological average characterizations were used in the Collection 2 processing of the Landsat TM data. The Landsat 1–5 MSS data were not atmospherically corrected in Collection 2 because of this issue and because the MSS carried only green, red and NIR bands. Simple but robust MSS atmospheric correction approaches may be merited for Collection 3, for example, by not correcting for aerosol scattering and absorption effects that optimally require blue and SWIR bands that the MSS did not carry. The NASA MODIS atmospheric characterization data used to atmospherically correct the Landsat 8 and 9 OLI data stream will need to be replaced when the NASA MODIS mission is retired (currently scheduled for late 2023/2024). Given the need for continuity of surface reflectance, studies to examine the impact of replacing the MODIS atmospheric characterization data with JPSS-1/2 VIIRS derived data have been undertaken, indicating minimal impacts (Fig. 9). The Landsat Next mission will include 15 new spectral bands (see for more information: https://landsat.gsfc.nasa.gov/satellites/landsat-next/) and several spectral bands will enable retrieval of atmospheric characteristics, such as aerosols and column water vapor. This will provide more contemporaneous atmospheric characterization data and so likely improved atmospheric correction and will reduce the processing latency by removing the need to wait for auxiliary atmospheric characterization data. The USGS plans to continue to examine the impact of auxiliary atmospheric correction data on the surface reflectance product performance, while also continuing to support new atmospheric correction research for Collection 3 and the Landsat Next mission.

The Landsat sensors are in sun-synchronous orbits acquiring near-nadir observations over narrow (about 15°) sensor field of views. Consequently, changes in the retrieved Landsat reflectance due only to changes in the solar and view geometry and surface reflectance anisotropy, described by the Bi-directional Reflectance Distribution Function (BRDF), have been considered negligible or smaller than residual atmospheric correction artefacts. The need to minimize BRDF effects became evident when large area Landsat mosaics started to be generated (Toivonen et al., 2006) and empirical BRDF minimization approaches were initially developed (Hansen et al., 2008). Subsequently, more sophisticated algorithms were developed and across-swath view zenith BRDF variations up to 0.02 and 0.06 (reflectance units) in the red and NIR Landsat bands were quantified (Roy et al., 2016). Unlike wide field-of-view daily coverage sensors, such as MODIS, Landsat does not provide sufficient angular sampling to characterize the BRDF reliably from the Landsat observations alone at time scales where the surface can be assumed to be unchanged (Roy et al., 2016). Consequently, semi-empirical algorithms have been developed to adjust Landsat reflectance to a nadir view, referred to as nadir-adjusted bidirectional reflectance (NBAR) (Roy et al., 2016; Zhang et al., 2018) using the MODIS BRDF product (Schaaf et al., 2002; Wang et al., 2018). Landsat NBAR has been shown to improve the consistency of Landsat time series

Table 6
Landsat Collection 2 Digital Object Identifiers (DOIs) and availability (month and year of first/last sensor data acquisition).

	LANDSAT 8/9 OLI/TIRS	LANDSAT 7 ETM+	LANDSAT 4/5 TM	LANDSAT 1–3 MSS
LEVEL 1	https://doi.org/10.5066/P975CC9B	https://doi.org/10.5066/P9TU80IG	https://doi.org/10.5066/P918ROHC	https://doi.org/10.5066/P9AF14YV
LEVEL 2	https://doi.org/10.5066/P9OGBGM6	https://doi.org/10.5066/P9C7I13B	https://doi.org/10.5066/P9IAXOVV	Currently Not Available
U.S. ARD	https://doi.org/10.5066/P960F8OC	https://doi.org/10.5066/P960F8OC	https://doi.org/10.5066/P960F8OC	Currently Not Available
AVAILABILITY	March 2013 to present	July 1999 to present	July 1982 to May 2012	July 1972 to October 1992

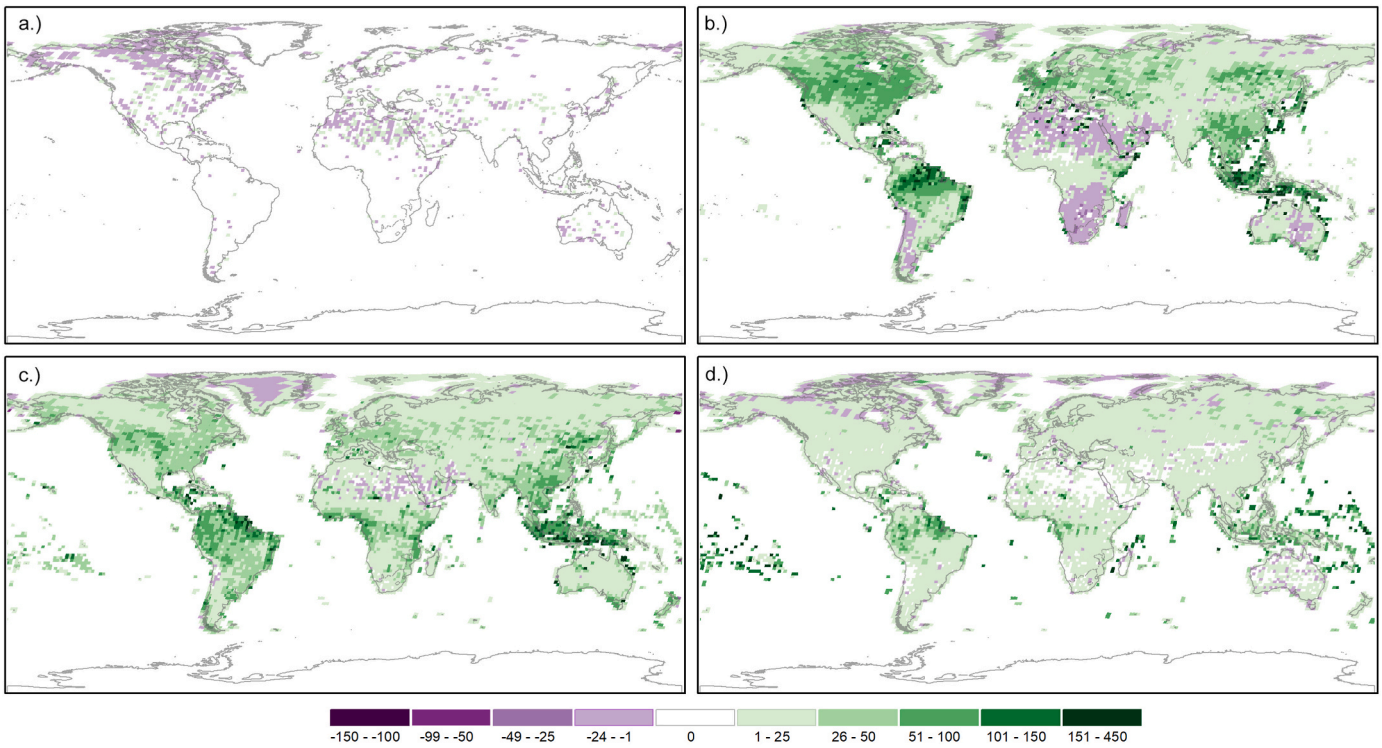

Fig. 8. Change in the total number of Landsat Level 1 Tier 1 images available in Collection 2 compared to Collection 1 considering a) MSS on Landsat 1–5 (for 1972–1983), b) TM on Landsat 4–5 (for 1982–2012), c) ETM + on Landsat 7 (for 1999–2021), and d) OLI/TIRS on Landsat 8 (for 2013–2021). The green colors represent an increase, and the purple colors indicate a decrease in the number (considering only daytime descending acquisitions).

(Qiu et al., 2018). However, this adjustment was not integrated into the Collection 2 processing, although Landsat users have begun to integrate it themselves for large area land cover mapping (Liu et al., 2021; Egorov et al., 2023; Zhang et al., 2023). The USGS expects to consider NBAR techniques for deployment as part of Collection 3 and in preparation for the Landsat Next mission.

The Landsat Level 2 surface temperature product is globally available and will be improved in Collection 3, with refinements supported by the results of product quality assessment and validation activities undertaken across a representative range of conditions and for the different Landsat sensor generations. The earlier Landsat missions carried no thermal infrared spectral bands (MSS) or only a single thermal infrared spectral band (TM and ETM+). Thus, there can be no MSS surface temperature product, and the Collection 2 TM and ETM + surface temperature products were necessarily derived using a single channel algorithm with the ASTER derived GEDv3 product to define the surface spectral emissivity. Prior to the Collection 2 processing there were no mature medium spatial resolution near global coverage surface emissivity datasets other than GEDv3. Future research to evaluate and develop new and more recent global spectral emissivity maps suitable for Collection 3 processing of the Landsat TM and ETM + data is recommended, for example, using emissivity data from more recent thermal satellites (Hulley et al., 2022) and improved resampling techniques to reduce boxy artefacts apparent in the Collection 2 surface temperature product. The Landsat TIRS sensors on both Landsat 8 and 9 carry two thermal infrared spectral bands. Consequently, improved surface temperature retrievals using both TIRS bands is recommended for Collection 3 to strengthen the utility of the Landsat surface temperature data record.

One of the hallmarks of Landsat Collection 1 was the ability to institutionalize the derivation of product quality assessment (QA) information as part of Landsat product generation (Dwyer et al., 2018). As evident from the MODIS land product suite (Justice et al., 1998; Roy et al., 2002), QA flags are essential to document the pixel-level scientific quality of products with respect to their intended performance, to document algorithm processing pathways and external factors (such as clouds) known to affect product quality and consistency. User examination of the Landsat product pixel QA information is warranted. The Landsat Collection 2 QA flags are stratified by processing levels where the amount of pixel level descriptive information increases progressively from Level 0 to Level 2. The Collection 2 strategy was to algorithmically process Level 1 and Level 2 data irrespective of QA condition to ensure that every pixel is processed consistently. Looking ahead to Collection 3, Level 1 cloud detection and screening and Level 2 atmospheric error propagation will be important areas for research and development. While the Landsat CFMask algorithm (used in Collections 1 and 2) outperformed other candidate cloud detection and screening algorithms in the first Cloud Masking Intercomparison Experiment (CMIX) (Skakun et al., 2022), more recent refinements have shown improved per-pixel results (Qiu et al., 2019, 2020) and new deep learning cloud masking algorithms show promise (Li et al., 2022). To facilitate Landsat-based cloud detection algorithm testing and intercomparison, the USGS has released several reference cloud mask validation datasets that have been derived using manual identification techniques (https://www.usgs.gov/landsat-missions/cloud-cover-assessment-validation-datasets).

There is an increasing recognition of the need for harmonized ARD generated using different sensor data. For example, the ESA Sentinel-2A/B data have similar characteristics as Landsat 8/9, and when used together, the data from both sensors provide improved temporal resolution (Li and Roy 2017). The processing steps to harmonize Landsat and Sentinel-2 reflectance data are complex and include adjustment of sensor spectral band pass differences, correction for BRDF effects, atmospheric correction using the same radiative transfer model and atmospheric characterization data, and reprojection into the same gridded coordinate system (Roy et al., 2019). This processing has been institutionalized and the NASA Harmonized Landsat Sentinel-2 (HLS) project generates Landsat and Sentinel-2 30 m data from 2015 onwards (Claverie et al., 2018), and the ESA Sen2Like project has developed

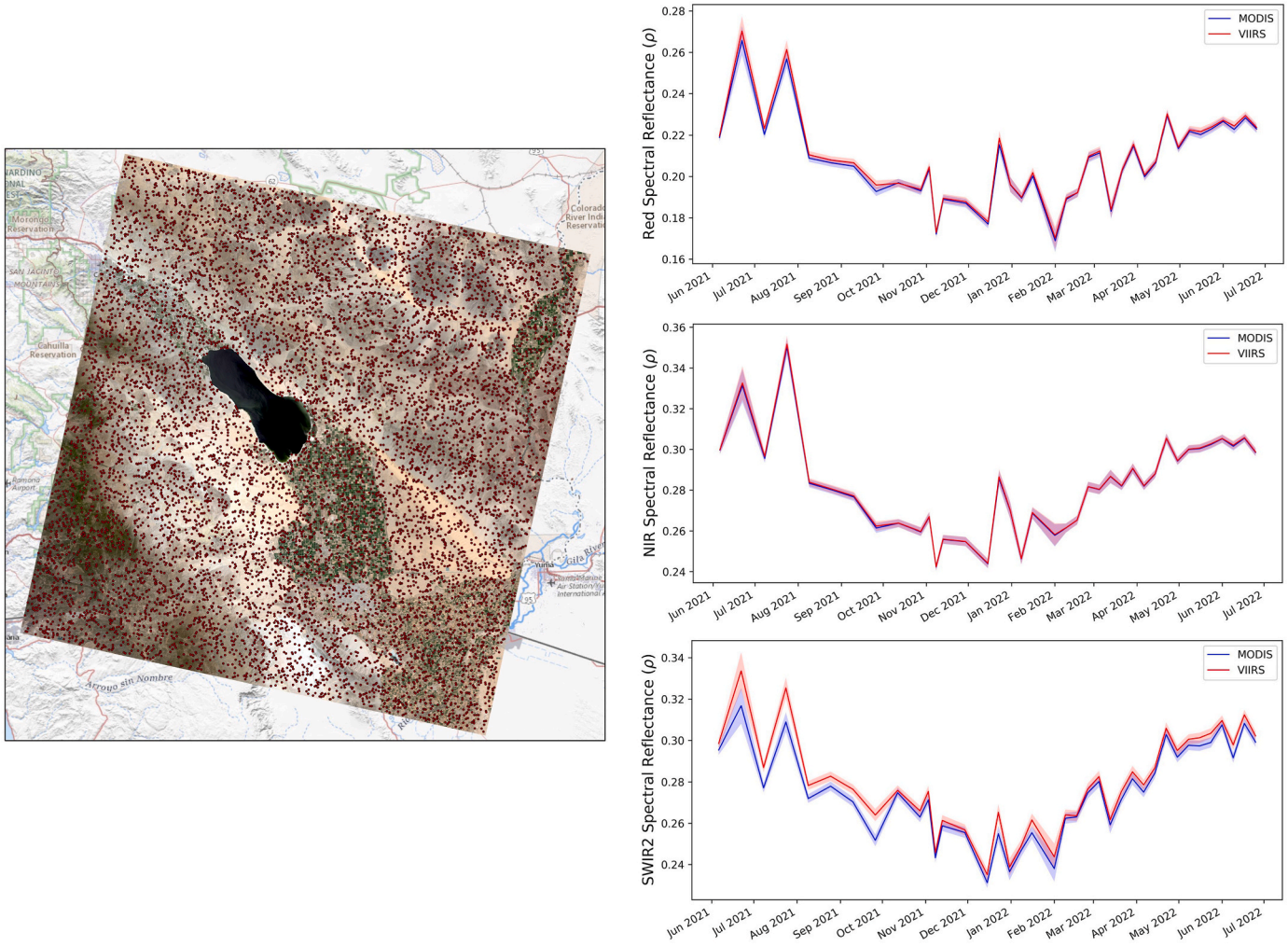

Fig. 9. Preliminary comparison of Collection 2 Level 2 OLI surface reflectance (June 2021 to June 2022) for the red, NIR, and SWIR2 bands that were atmospherically corrected independently using MODIS Terra and using JPSS 2 VIIRS climate modelling grid (CMG) atmospheric auxiliary data. Results derived considering 10,000 randomly selected land pixels over the Salton Sea, California (land pixel locations shown by red dots in the left Landsat image).

algorithms to generate harmonized 10 m Landsat and Sentinel-2 products (Saunier et al., 2022). Production of consistent multi-sensor ARD will benefit from the availability of collection-based processing, particularly if future Landsat and Sentinel-2 collection processing schedules are synchronized.

The Collection 3 schedule has not yet been set but will likely occur before or in synchronization with the planned Landsat Next mission while allowing time for users to become familiar with the Collection 2 products that have been available since December 2020. Certainly, the Collection 3 schedule is not computationally constrained - the barriers to rapid processing of the global Landsat archive were significantly reduced from Collection 1 (18 months) to Collection 2 (5 weeks) by the adoption of commercial cloud processing. The Collection 3 schedule will also be contingent on the results of Collection 2 product quality assessment and validation activities and the development time for any needed algorithm refinements. Refinements to ensure the provision of Landsat 1–9 data that are consistent with the Landsat Next mission data may also be expected.

6. Conclusion

This paper overviewed the rationale for the Landsat Collection 2 processing and improvements over Collection 1, highlighted the new global coverage surface reflectance and temperature products, and outlined the likely improvements expected in the Landsat Collection 3 processing. The Landsat data record provides more than 50 years of global terrestrial observations that continues with the Landsat 8 and 9 data streams. Landsat Collection 2 provides greater radiometric consistency and improved geolocation needed for time series analyses and is an important step forward in enabling science and applications and fusion with other satellite data. Landsat users can migrate their science and applications to using the Collection 2 products since the Collection 1 products were removed from public distribution on December 31, 2022. The suite of USGS Landsat 1–9 Collection 2 products are available for download (https://earthexplorer.usgs.gov) or direct access in the USGS managed AWS commercial cloud (https://registry.opendata.aws/usgs-landsat/).

Funding

This research was funded by the USGS Core Science Systems Mission Area and National Land Imaging programs via Land Satellite Data Systems Research and Development project (GX23ED00EDK1A00), NASA Landsat 9 Phase E project, and USGS Landsat Science Team support services contract (G12PC00069). KBR performed work under contract number (140G0121D001).

Declaration of competing interest

The authors declare that they have no known competing financial interests or personal relationships that could have appeared to influence the work reported in this paper.

Data availability

The Landsat data is publicly available for access and links have been provided in the manuscript text.

Acknowledgements

The USGS Landsat program management and staff are thanked for the open access and no-cost Landsat data, and their resources and energy in supporting the development of the Landsat Collection 2 products. Any use of trade, firm, or product names is for descriptive purposes only and does not imply endorsement by the U.S. Government.

References

Barsi, J., Schott, J., Hook, S., Raqueno, N., Markham, B., Radocinski, R., 2014. Landsat-8 thermal infrared sensor (TIRS) vicarious radiometric calibration. Rem. Sens. 6, 11607–11626. https://doi.org/10.3390/rs61111607.

Barsi, J.A., Markham, B.L., Montanaro, M., Hook, S., Raqueño, N., Miller, J.A., Willette, R., 2020. Landsat-8 TIRS radiometric calibration status. In: Proc. SPIE 11501, Earth Observing Systems XXV. Society of Photo-Optical Instrumentation Engineers, Bellingham, WA, 115010L. https://doi.org/10.1117/12.2567807.

Barsi, J.A., Montanaro, M., Thome, K.L., Raqueno, N.G., Hook, S., Anderson, C.H., Micijevic, E., 2022. Early radiometric performance of landsat-9 thermal infrared sensor. In: Proc. SPIE 12232, Earth Observing Systems XXVII. Society of Photo-Optical Instrumentation Engineers, Belllingham, WA, 122320u. https://doi.org/10.1117/12.2634058.

Brooks, E.B., Wynne, R.H., Thomas, V.A., 2018. Using window regression to gap-fill Landsat ETM+ post SLC-Off data. Rem. Sens. 10 (10), 1502.

Brown, J.F., Tollerud, H.J., Barber, C.P., Zhou, Q., Dwyer, J.L., Vogelmann, J.E., Loveland, T.R., Woodcock, C.E., Stehman, S.V., Zhu, Z., Pengra, B.W., Smith, K., Horton, J.A., Xian, G., Auch, R.F., Sohl, T.L., Sayler, K.L., Gallant, A.L., Zelenak, D., Reker, R.R., Rover, J., 2020. Lessons learned implementing an operational continuous United States national land change monitoring capability: the land change monitoring, assessment, and projection (LCMAP) approach. Remote Sens. Environ. 238, 111356 https://doi.org/10.1016/j.rse.2019.111356.

Chavez Jr., P.S., 1996. Image-based atmospheric corrections—revisited and improved. Photogramm. Eng. Rem. Sens. 62, 1025–1036.

Claverie, M., Ju, J., Masek, J.G., Dungan, J.L., Vermote, E.F., Roger, J.C., et al., 2018. The Harmonized Landsat and Sentinel-2 surface reflectance data set. Rem. Sens. Environ. 219, 145–161.

Cook, M., Schott, J., Mandel, J., Raqueno, N., 2014. Development of an operational calibration methodology for the Landsat thermal data archive and initial testing of the atmospheric compensation component of a land surface temperature (LST) product from the archive. Rem. Sens. 6, 11244–11266. https://doi.org/10.3390/rs61111244.

Doxani, G., Vermote, E.F., Roger, J.C., Skakun, S., Gascon, F., Collison, A., De Keukelaere, L., Desjardins, C., Frantz, D., Hagolle, O., Kim, M., Louis, J., Pacifici, F., Pflug, B., Poilvé, H., Ramon, D., Richter, R., Yin, F., 2023. Atmospheric Correction Inter-comparison eXercise, ACIX-II Land—an assessment of atmospheric correction processors for Landsat 8 and Sentinel-2 over land. Remote Sens. Environ. 285, 113412 https://doi.org/10.1016/j.rse.2022.113412.

Dwyer, J.L., Roy, D.P., Sauer, B., Jenkerson, C.B., Zhang, H.K., Lymburner, L., 2018. Analysis ready data: enabling analysis of the Landsat archive. Rem. Sens. 10, 1363. https://doi.org/10.3390/rs10091363.

Egorov, A., Roy, D.P., Boschetti, L., 2023. Generation and comprehensive validation of 30 m conterminous United States Landsat percent tree cover and forest cover loss annual products. Sci. Remote Sens. 7, 100084 https://doi.org/10.1016/j.srs.2023.100084.

Fahnestock, M., Scambos, T., Moon, T., Gardner, A., Haran, T., Klinger, M., 2016. Rapid large-area mapping of ice flow using Landsat 8. Remote Sens. Environ. 185, 84–94. https://doi.org/10.1016/j.rse.2015.11.023.

Feng, M., Sexton, J.O., Huang, C., Masek, J.G., Vermote, E.F., Gao, F., Narasimhan, R., Channan, S., Wolfe, R.E., Townshend, J.R., 2013. Global surface reflectance products from Landsat: assessment using coincident MODIS observations. Remote Sens. Environ. 134, 276–293. https://doi.org/10.1016/j.rse.2013.02.031.

Foga, S., Scaramuzza, P.L., Guo, S., Zhu, Z., Dilley, R.D., Beckmann, T., Schmidt, G.L., Dwyer, J.L., Joseph Hughes, M., Laue, B., 2017. Cloud detection algorithm comparison and validation for operational Landsat data products. Remote Sens. Environ. 194, 379–390. https://doi.org/10.1016/j.rse.2017.03.026.

Franks, S., Storey, J., Rengarajan, R., 2020. The new Landsat collection-2 digital elevation model. Rem. Sens. 12, 3909. https://doi.org/10.3390/rs12233909.

Gelaro, R., McCarty, W., Suárez, M.J., Todling, R., Molod, A., Takacs, L., Randles, C., Darmenov, A., Bosilovich, M.G., Reichle, R., Wargan, K., Coy, L., Cullather, R., Draper, C., Akella, S., Buchard, V., Conaty, A., da Silva, A., Gu, W., Kim, G.-K., Koster, R., Lucchesi, R., Merkova, D., Nielsen, J.E., Partyka, G., Pawson, S., Putman, W., Rienecker, M., Schubert, S.D., Sienkiewicz, M., Zhao, B., 2017. The Modern-Era Retrospective analysis for research and applications, version 2 (MERRA-2). J. Clim. 30, 5419–5454. https://doi.org/10.1175/JCLI-D-16-0758.1.

Gerace, A., Kleynhans, T., Eon, R., Montanaro, M., 2020. Towards an operational, split window-derived surface temperature product for the thermal infrared sensors onboard Landsat 8 and 9. Rem. Sens. 12, 224. https://doi.org/10.3390/rs12020224.

Gerace, A., Montanaro, M., 2017. Derivation and validation of the stray light correction algorithm for the Thermal Infrared Sensor onboard Landsat 8. Remote Sens. Environ. 191, 246–257. https://doi.org/10.1016/j.rse.2017.01.029.

Gerace, A., Montanaro, M., Beckmann, T., Tyrrell, K., Cozzo, A., Carney, T., Ngan, V., 2015. TIRS stray light correction: algorithms and performance. In: Proc. SPIE 9607, Earth Observing Systems XX. Society of Photo-Optical Instrumentation Engineers, Bellingham, WA, p. 96070Q. https://doi.org/10.1117/12.2188862.

Goward, S.N., Rocchio, L.E.P., Williams, D.L., Arvidson, T., Irons, J.R., Russell, C.A., Johnston, S.S., 2017. Landsat's Enduring Legacy: Pioneering Global Land Observations from Space. American Society for Photogrammetry and Remote Sensing, Bethesda, MD. https://doi.org/10.14358/asprs.1.57083.101.7.

Gross, G., Helder, D., Begeman, C., Leigh, L., Kaewmanee, M., Shah, R., 2022. Initial cross-calibration of Landsat 8 and Landsat 9 using the simultaneous underfly event. Rem. Sens. 14, 2418. https://doi.org/10.3390/rs14102418.

Gutman, G., Huang, C., Chander, G., Noojipady, P., Masek, J.G., 2013. Assessment of the NASA–USGS global land Survey (GLS) datasets. Remote Sens. Environ. 134, 249–265. https://doi.org/10.1016/j.rse.2013.02.026.

Hansen, M.C., Roy, D.P., Lindquist, E., Adusei, B., Justice, C.O., Altstatt, A., 2008. A method for integrating MODIS and Landsat data for systematic monitoring of forest cover and change in the Congo Basin. Remote Sens. Environ. 112, 2495–2513. https://doi.org/10.1016/j.rse.2007.11.012.

Helder, D.L., Ruggles, T.A., Dewald, J.D., Madhavan, S., 2004. Landsat-5 Thematic Mapper reflective-band radiometric stability. IEEE Trans. Geosci. Rem. Sens. 42, 2730–2746. https://doi.org/10.1109/tgrs.2004.839088.

Hook, S.J., Chander, G., Barsi, J.A., Alley, R.E., Abtahi, A., Palluconi, F.D., Markham, B. L., Richards, R.C., Schladow, S.G., Helder, D.L., 2004. In-flight validation and recovery of water surface temperature with Landsat-5 thermal infrared data using an automated high-altitude lake validation site at Lake Tahoe. IEEE Trans. Geosci. Rem. Sens. 42, 2767–2776. https://doi.org/10.1109/tgrs.2004.839092.

Hulley, G.C., Gottsche, F.M., Rivera, G., Hook, S.J., Freepartner, R.J., Martin, M.A., Cawse-Nicholson, K., Johnson, W.R., 2022. Validation and quality assessment of the ECOSTRESS level-2 land surface temperature and emissivity product. IEEE Trans. Geosci. Rem. Sens. 60, 1–23. https://doi.org/10.1109/tgrs.2021.3079879.

Hulley, G.C., Hook, S.J., Abbott, E., Malakar, N., Islam, T., Abrams, M., 2015. The ASTER global emissivity dataset (ASTER GED): mapping earth's emissivity at 100 meter spatial scale. Geophys. Res. Lett. 42, 7966–7976. https://doi.org/10.1002/2015gl065564.

Irish, R.R., Barker, J.L., Goward, S.N., Arvidson, T., 2006. Characterization of the Landsat-7 ETM+ automated cloud-cover assessment (ACCA) algorithm. Photogramm. Eng. Rem. Sens. 72, 1179–1188. https://doi.org/10.14358/PERS.72.10.1179.

Johnson, D.M., Mueller, R., 2010. The 2009 cropland data layer. Photogramm. Eng. Rem. Sens. 76, 1201–1205.

Ju, J., Roy, D.P., Vermote, E.F., Masek, J.G., Kovalskyy, V., 2012. Continental-scale validation of MODIS-based and LEDAPS Landsat ETM+ atmospheric correction methods. Remote Sens. Environ. 122, 175–184. https://doi.org/10.1016/j.rse.2011.12.025.

Justice, C.O., Townshend, J.R.G., Vermote, E.F., Masuoka, E., Wolfe, R.E., Saleous, N., Roy, D.P., Morisette, J.T., 2002. An overview of MODIS Land data processing and product status. Remote Sens. Environ. 83, 3–15. https://doi.org/10.1016/s0034-4257(02)00084-6.

Justice, C.O., Vermote, E., Townshend, J.R.G., Defries, R., Roy, D.P., Hall, D.K., Salomonson, V.V., Privette, J.L., Riggs, G., Strahler, A., Lucht, W., Myneni, R.B., Knyazikhin, Y., Running, S.W., Nemani, R.R., Zhengming, W., Huete, A.R., van Leeuwen, W., Wolfe, R.E., Giglio, L., Muller, J., Lewis, P., Barnsley, M.J., 1998. The Moderate Resolution Imaging Spectroradiometer (MODIS): land remote sensing for global change research. IEEE Trans. Geosci. Rem. Sens. 36, 1228–1249. https://doi.org/10.1109/36.701075.

Kaita, E., Markham, B., Haque, M.O., Dichmann, D., Gerace, A., Leigh, L., Good, S., Schmidt, M., Crawford, C.J., 2022. Landsat 9 cross calibration under-fly of Landsat 8: planning, and execution. Rem. Sens. 14, 5414. https://doi.org/10.3390/rs14215414.

Kotchenova, S.Y., Vermote, E.F., Matarrese, R., Klemm Jr., F.J., 2006. Validation of a vector version of the 6S radiative transfer code for atmospheric correction of satellite data. Part I: path radiance. Appl. Opt. 45, 6762–6774. https://doi.org/10.1364/AO.45.006762.

Kovalskyy, V., Roy, D.P., 2013. The global availability of Landsat 5 TM and Landsat 7 ETM+ land surface observations and implications for global 30m Landsat data product generation. Remote Sens. Environ. 130, 280–293. https://doi.org/10.1016/j.rse.2012.12.003.

Kovalskyy, V., Roy, D.P., 2015. A one-year Landsat 8 conterminous United States study of cirrus and non-cirrus clouds. Rem. Sens. 7, 564–578. https://doi.org/10.3390/rs70100564.

Laraby, K.G., Schott, J.R., 2018. Uncertainty estimation method and Landsat 7 global validation for the Landsat surface temperature product. Remote Sens. Environ. 216, 472–481. https://doi.org/10.1016/j.rse.2018.06.026.

Li, J., Roy, D.P., 2017. A global analysis of Sentinel-2A, Sentinel-2B and Landsat-8 data revisit intervals and implications for terrestrial monitoring. Rem. Sens. 9 (9), 902.

Li, Z., Zhang, H.K., Roy, D.P., Yan, L., Huang, H., Li, J., 2017. Landsat 15-m Panchromatic-Assisted Downscaling (LPAD) of the 30-m reflective wavelength bands to Sentinel-2 20-m resolution. Rem. Sens. 9, 755. https://doi.org/10.3390/rs9070755.

Li, Z., Shen, H., Weng, Q., Zhang, Y., Dou, P., Zhang, L., 2022. Cloud and cloud shadow detection for optical satellite imagery: features, algorithms, validation, and prospects. ISPRS J. Photogrammetry Remote Sens. 188, 89–108. https://doi.org/10.1016/j.isprsjprs.2022.03.020.

Liang, S., Fang, H., Chen, M., 2001. Atmospheric correction of Landsat ETM+ land surface imagery. I. Methods. IEEE Trans. Geosci. Remote Sens. 39, 2490–2498. https://doi.org/10.1109/36.964986.

Liu, H., Gong, P., Wang, J., Wang, X., Ning, G., Xu, B., 2021. Production of global daily seamless data cubes and quantification of global land cover change from 1985 to 2020 - iMap World 1.0. Remote Sens. Environ. 258, 112364 https://doi.org/10.1016/j.rse.2021.112364.

Lucchesi, R., 2017. File Specification for GEOS-5 FP. GMAO Office Note No. 4. NASA Goddard Spaceflight Center, Greenbelt, MD. Version 1.1).

Loveland, T.R., Dwyer, J.L., 2012. Landsat—building a strong future. Remote Sens. Environ. 122, 22–29. https://doi.org/10.1016/j.rse.2011.09.022.

Maiersperger, T.K., Scaramuzza, P.L., Leigh, L., Shrestha, S., Gallo, K.P., Jenkerson, C.B., Dwyer, J.L., 2013. Characterizing LEDAPS surface reflectance products by comparisons with AERONET, field spectrometer, and MODIS data. Remote Sens. Environ. 136, 1–13. https://doi.org/10.1016/j.rse.2013.04.007.

Malakar, N.K., Hulley, G.C., Hook, S.J., Laraby, K., Cook, M., Schott, J.R., 2018. An operational land surface temperature product for Landsat thermal data: methodology and validation. IEEE Trans. Geosci. Rem. Sens. 56, 5717–5735. https://doi.org/10.1109/tgrs.2018.2824828.

Markham, B.L., Storey, J.C., Williams, D.L., Irons, J.R., 2004a. Landsat sensor performance: history and current status. IEEE Trans. Geosci. Rem. Sens. 42 (12), 2691–2694.

Markham, B.L., Barsi, J.A., Kaita, E., Ong, L., Morfitt, R.A., Haque, M.O., 2015. Radiometric calibration and stability of the landsat-8 operational land imager (OLI). In: Proc. SPIE 9607, Earth Observing Systems XX. Society of Photo-Optical Instrumentation Engineers, Bellingham, WA, 96070N. https://doi.org/10.1117/12.2188412.

Markham, B., Barsi, J., Kvaran, G., Ong, L., Kaita, E., Biggar, S., Czapla-Myers, J., Mishra, N., Helder, D., 2014. Landsat-8 operational land imager radiometric calibration and stability. Rem. Sens. 6, 12275–12308. https://doi.org/10.3390/rs61212275.

Markham, B.L., Thome, K.J., Barsi, J.A., Kaita, E., Helder, D.L., Barker, J.L., Scaramuzza, P.L., 2004b. Landsat-7 ETM+ on-orbit reflective-band radiometric stability and absolute calibration. IEEE Trans. Geosci. Rem. Sens. 42, 2810–2820. https://doi.org/10.1109/tgrs.2004.836389.

Masek, J.G., Vermote, E.F., Saleous, N.E., Wolfe, R., Hall, F.G., Huemmrich, K.F., Gao, F., Kutler, J., Lim, T.K., 2006. A Landsat surface reflectance dataset for North America, 1990–2000. IEEE Trans. Geosci. Remote Sens. Lett. 3, 68–72. https://doi.org/10.1109/lgrs.2005.857030.

Masek, J.G., Wulder, M.A., Markham, B., McCorkel, J., Crawford, C.J., Storey, J., Jenstrom, D.T., 2020. Landsat 9: empowering open science and applications through continuity. Remote Sens. Environ. 248, 111968 https://doi.org/10.1016/j.rse.2020.111968.

Masuoka, E., Roy, D.P., Wolfe, R., Morisette, J., Sinno, S., Teague, M., Saleous, N., Devadiga, S., Justice, C.O., Nickeson, J., 2011. MODIS land data products—generation, quality assurance and validation. In: Ramachandran, B., Justice, C.O., Abrams, M.J. (Eds.), Land Remote Sensing and Global Environmental Change. Springer, New York, NY, pp. 509–531. https://doi.org/10.1007/978-1-4419-6749-7_22.

Micijevic, E., Barsi, J., Haque, M.O., Levy, R., Anderson, C., Thome, K., Czapla-Myers, J., Helder, D., 2022. Radiometric performance of the Landsat 9 operational land imager over the first 8 months on orbit. In: Proc. SPIE 12232, Earth Observing Systems XXVII. Society of Photo-Optical Instrumentation Engineers, Bellingham, WA, p. 122320w. https://doi.org/10.1117/12.2634301.

Micijevic, E., Haque, M.O., Barsi, J.A., Anderson, C., Markham, B.L., Rengarajan, R., 2020. Landsat Collection 2 radiometric calibration updates. In: Proc. SPIE 11501, Earth Observing Systems XXV. Society of Photo-Optical Instrumentation Engineers, Bellingham, WA, 115010M. https://doi.org/10.1117/12.2570026.

Micijevic, E., Haque, M.O., Mishra, N., 2017. Radiometric characterization of Landsat collection 1 products. In: Proc. SPIE 10402, Earth Observing Systems XXII. Society of Photo-Optical Instrumentation Engineers, Bellingham, WA, 104021D. https://doi.org/10.1117/12.2276065.

Micijevic, E., Haque, M.O., Scaramuzza, P., Storey, J., Anderson, C., Markham, B., 2019. Landsat 9 pre-launch sensor characterization and comparison with Landsat 8 results. In: Proc. SPIE 11151, Sensors, Systems, and Next-Generation Satellites XXIII. Society of Photo-Optical Instrumentation Engineers, Bellingham, WA, p. 111511F. https://doi.org/10.1117/12.2533102.

Mishra, N., Helder, D., Barsi, J., Markham, B., 2016. Continuous calibration improvement: Landsat 5 through Landsat 8. Remote Sens. Environ. 185, 7–15. https://doi.org/10.1016/j.rse.2016.07.032.

Montanaro, M., Gerace, A., Lunsford, A., Reuter, D., 2014. Stray light artifacts in imagery from the Landsat 8 thermal infrared sensor. Rem. Sens. 6, 10435–10456. https://doi.org/10.3390/rs61110435.

Nazeer, M., Nichol, J.E., Yung, Y.-K., 2014. Evaluation of atmospheric correction models and Landsat surface reflectance product in an urban coastal environment. Int. J. Rem. Sens. 35, 6271–6291. https://doi.org/10.1080/01431161.2014.951742.

Ouaidrari, H., Vermote, E.F., 1999. Operational atmospheric correction of Landsat TM data. Remote Sens. Environ. 70, 4–15. https://doi.org/10.1016/S0034-4257(99)00054-1.

Pahlevan, N., Schott, J.R., Franz, B.A., Zibordi, G., Markham, B., Bailey, S., Schaaf, C.B., Ondrusek, M., Greb, S., Strait, C.M., 2017. Landsat 8 remote sensing reflectance (Rrs) products: evaluations, intercomparisons, and enhancements. Remote Sens. Environ. 190, 289–301. https://doi.org/10.1016/j.rse.2016.12.030.

Qiu, S., Lin, Y., Shang, R., Zhang, J., Ma, L., Zhu, Z., 2018. Making Landsat time series consistent: evaluating and improving Landsat analysis ready data. Rem. Sens. 11, 51. https://doi.org/10.3390/rs11010051.

Qiu, S., Zhu, Z., He, B., 2019. Fmask 4.0: improved cloud and cloud shadow detection in Landsats 4–8 and Sentinel-2 imagery. Remote Sens. Environ. 231, 111205 https://doi.org/10.1016/j.rse.2019.05.024.

Qiu, S., Zhu, Z., Woodcock, C.E., 2020. Cirrus clouds that adversely affect Landsat 8 images: what are they and how to detect them? Remote Sens. Environ. 246, 111884 https://doi.org/10.1016/j.rse.2020.111884.

Rengarajan, R., Storey, J.C., Choate, M.J., 2020. Harmonizing the Landsat ground reference with the Sentinel-2 global reference image using space-based bundle adjustment. Rem. Sens. 12, 3132. https://doi.org/10.3390/rs12193132.

Reuter, D., Richardson, C., Pellerano, F., Irons, J., Allen, R., Anderson, M., Jhabvala, M., Lunsford, A., Montanaro, M., Smith, R., Tesfaye, Z., Thome, K., 2015. The thermal infrared sensor (TIRS) on Landsat 8: design overview and pre-launch characterization. Rem. Sens. 7, 1135–1153. https://doi.org/10.3390/rs70101135.

Roger, J.C., Vermote, E., Skakun, S., Murphy, E., Dubovik, O., Kalecinski, N., Korgo, B., Holben, B., 2022. Aerosol models from the AERONET database—application to surface reflectance validation. Atmos. Meas. Tech. 15, 1123–1144. https://doi.org/10.5194/amt-15-1123-2022.

Roy, D.P., Borak, J.S., Devadiga, S., Wolfe, R.E., Zheng, M., Descloitres, J., 2002. The MODIS Land Product quality assessment approach. Remote Sens. Environ. 83, 62–76. https://doi.org/10.1016/s0034-4257(02)00087-1.

Roy, D.P., Ju, J., Kline, K., Scaramuzza, P.L., Kovalskyy, V., Hansen, M., Loveland, T.R., Vermote, E., Zhang, C., 2010. Web-enabled Landsat data (WELD): Landsat ETM+ composited mosaics of the conterminous United States. Remote Sens. Environ. 114, 35–49. https://doi.org/10.1016/j.rse.2009.08.011.

Roy, D.P., Wulder, M.A., Loveland, T.R., C.E, W., Allen, R.G., Anderson, M.C., Helder, D., Irons, J.R., Johnson, D.M., Kennedy, R., Scambos, T.A., Schaaf, C.B., Schott, J.R., Sheng, Y., Vermote, E.F., Belward, A.S., Bindschadler, R., Cohen, W.B., Gao, F., Hipple, J.D., Hostert, P., Huntington, J., Justice, C.O., Kilic, A., Kovalskyy, V., Lee, Z. P., Lymburner, L., Masek, J.G., McCorkel, J., Shuai, Y., Trezza, R., Vogelmann, J., Wynne, R.H., Zhu, Z., 2014. Landsat-8: science and product vision for terrestrial global change research. Remote Sens. Environ. 145, 154–172. https://doi.org/10.1016/j.rse.2014.02.001.

Roy, D.P., Zhang, H.K., Ju, J., Gomez-Dans, J.L., Lewis, P.E., Schaaf, C.B., Sun, Q., Li, J., Huang, H., Kovalskyy, V., 2016. A general method to normalize Landsat reflectance data to nadir BRDF adjusted reflectance. Remote Sens. Environ. 176, 255–271. https://doi.org/10.1016/j.rse.2016.01.023.

Roy, D.P., Huang, H., Boschetti, L., Giglio, L., Yan, L., Zhang, H.H., Li, Z., 2019. Landsat-8 and Sentinel-2 burned area mapping-A combined sensor multi-temporal change detection approach. Rem. Sens. Environ. 231, 111254.

Saunier, S., Pflug, B., Lobos, I.M., Franch, B., Louis, J., De Los Reyes, R., et al., 2022. Sen2Like: paving the way towards harmonization and fusion of optical data. Rem. Sens. 14 (16), 3855.

Scambos, T.A., Campbell, G.G., Pope, A., Haran, T., Muto, A., Lazzara, M., Reijmer, C.H., Van den Broeke, M.R., 2018. Ultralow surface temperatures in East Antarctica from satellite thermal infrared mapping: the coldest places on Earth. Geophys. Res. Lett. 45, 6124–6133. https://doi.org/10.1029/2018GL078133.

Schaaf, C.B., Gao, F., Strahler, A.H., Lucht, W., Li, X., Tsang, T., Strugnell, N.C., Zhang, X., Jin, Y., Muller, J.-P., Lewis, P., Barnsley, M., Hobson, P., Disney, M., Roberts, G., Dunderdale, M., Doll, C., d'Entremont, R.P., Hu, B., Liang, S., Privette, J. L., Roy, D., 2002. First operational BRDF, albedo nadir reflectance products from MODIS. Remote Sens. Environ. 83, 135–148. https://doi.org/10.1016/s0034-4257(02)00091-3.

Schaepman-Strub, G., Schaepman, M.E., Painter, T.H., Dangel, S., Martonchik, J.V., 2006. Reflectance quantities in optical remote sensing-definitions and case studies. Remote Sens. Environ. 103, 27–42. https://doi.org/10.1016/j.rse.2006.03.002.

Schott, J.R., Gerace, A., Raqueno, N., Ientilucci, E., Raqueno, R., Lunsford, A.W., 2014. Chasing the TIRS ghosts: calibrating the Landsat 8 thermal bands. In: Proc. SPIE 9218, Earth Observing Systems XIX. Society of Photo-Optical Instrumentation Engineers, Bellingham, WA, p. 92181A. https://doi.org/10.1117/12.2063236.

Schott, J.R., Hook, S.J., Barsi, J.A., Markham, B.L., Miller, J., Padula, F.P., Raqueno, N. G., 2012. Thermal infrared radiometric calibration of the entire Landsat 4, 5, and 7 archive (1982–2010). Remote Sens. Environ. 122, 41–49. https://doi.org/10.1016/j.rse.2011.07.022.

Shlien, S., 1979. Geometric correction, registration, and resampling of Landsat imagery. Can. J. Rem. Sens. 5, 74–89. https://doi.org/10.1080/07038992.1979.10854986.

Skakun, S., Vermote, E.F., Roger, J.C., Justice, C.O., Masek, J.G., 2019. Validation of the LaSRC cloud detection algorithm for Landsat 8 images. IEEE J. Sel. Top. Appl. Earth Obs. Rem. Sens. 12, 2439–2446. https://doi.org/10.1109/JSTARS.2019.2894553.

Skakun, S., Wevers, J., Brockmann, C., Doxani, G., Aleksandrov, M., Batič, M., Frantz, D., Gascon, F., Gómez-Chova, L., Hagolle, O., López-Puigdollers, D., Louis, J., Lubej, M., Mateo-García, G., Osman, J., Peressutti, D., Pflug, B., Puc, J., Richter, R., Roger, J.-C., Scaramuzza, P., Vermote, E., Vesel, N., Zupanc, A., Žust, L., 2022. Cloud Mask Intercomparison eXercise (CMIX): an evaluation of cloud masking algorithms for Landsat 8 and Sentinel-2. Remote Sens. Environ. 274, 112990 https://doi.org/10.1016/j.rse.2022.112990.

Storey, J., Roy, D.P., Masek, J., Gascon, F., Dwyer, J., Choate, M., 2016. A note on the temporary misregistration of landsat-8 operational land imager (OLI) and sentinel-2 multi spectral instrument (MSI) imagery. Remote Sens. Environ. 186, 121–122. https://doi.org/10.1016/j.rse.2016.08.025.

Storey, J.C., Choate, M.J., 2004. Landsat-5 bumper-mode geometric correction. IEEE Trans. Geosci. Rem. Sens. 42, 2695–2703. https://doi.org/10.1109/tgrs.2004.836390.

Storey, J.C., Rengarajan, R., Choate, M.J., 2019. Bundle adjustment using space-based triangulation method for improving the Landsat global ground reference. Rem. Sens. 11, 1640. https://doi.org/10.3390/rs11141640.

Tanré, D., Deroo, C., Duhaut, P., Herman, M., Morcrette, J.J., Perbos, J., Deschamps, P. Y., 1990. Technical note Description of a computer code to simulate the satellite signal in the solar spectrum: the 5S code. Int. J. Rem. Sens. 11, 659–668. https://doi.org/10.1080/01431169008955048.

Toivonen, T., Kalliola, R., Ruokolainen, K., Naseem Malik, R., 2006. Across-path DN gradient in Landsat TM imagery of Amazonian forests: a challenge for image interpretation and mosaicking. Remote Sens. Environ. 100, 550–562. https://doi.org/10.1016/j.rse.2005.11.006.

Tonooka, H., 2005. Accurate atmospheric correction of ASTER thermal infrared imagery using the WVS method. IEEE Trans. Geosci. Rem. Sens. 43, 2778–2792. https://doi.org/10.1109/tgrs.2005.857886.

Vermote, E., Justice, C., Claverie, M., Franch, B., 2016. Preliminary analysis of the performance of the Landsat 8/OLI land surface reflectance product. Remote Sens. Environ. 185, 46–56. https://doi.org/10.1016/j.rse.2016.04.008.

Vermote, E., McCorkel, J., Rountree, W.H., Santamaria-Artigas, A., Skakun, S., Franch, B., Roger, J.C., 2022. Validation of high spatial resolution surface reflectance using a camera system (CAMSIS). In: IGARSS 2022 - 2022 IEEE International Geoscience and Remote Sensing Symposium. Kuala Lumpur, Malaysia, pp. 7729–7732. https://doi.org/10.1109/IGARSS46834.2022.9883241.

Vuolo, F., Mattiuzzi, M., Atzberger, C., 2015. Comparison of the Landsat Surface Reflectance Climate Data Record (CDR) and manually atmospherically corrected data in a semi-arid European study area. Int. J. Appl. Earth Obs. Geoinf. 42, 1–10. https://doi.org/10.1016/j.jag.2015.05.003.

Wan, Z., Dozier, J., 1996. A generalized split-window algorithm for retrieving land-surface temperature from space. IEEE Trans. Geosci. Rem. Sens. 34, 892–905. https://doi.org/10.1109/36.508406.

Wang, Z., Schaaf, C.B., Sun, Q., Shuai, Y., Román, M.O., 2018. Capturing rapid land surface dynamics with Collection V006 MODIS BRDF/NBAR/Albedo (MCD43) products. Remote Sens. Environ. 207, 50–64. https://doi.org/10.1016/j.rse.2018.02.001.

Wang, Q., Wang, L., Li, Z., Tong, X., Atkinson, P.M., 2020. Spatial–spectral radial basis function-based interpolation for Landsat ETM+ SLC-off image gap filling. IEEE Trans. Geosci. Rem. Sens. 59 (9), 7901–7917.

Wickham, J., Stehman, S.V., Sorenson, D.G., Gass, L., Dewitz, J.A., 2021. Thematic accuracy assessment of the NLCD 2016 land cover for the conterminous United States. Remote Sens. Environ. 257, 112357 https://doi.org/10.1016/j.rse.2021.112357.

Williams, R.S., Carter, W.D., 1976. ERTS-1, a New Window on Our Planet. U.S. Geological Survey, Reston, VA. https://doi.org/10.3133/pp929. Professional Paper 929.

Wolfe, R.E., Roy, D.P., Vermote, E., 1998. MODIS land data storage, gridding, and compositing methodology: level 2 grid. IEEE Trans. Geosci. Rem. Sens. 36, 1324–1338. https://doi.org/10.1109/36.701082.

Wulder, M.A., Loveland, T.R., Roy, D.P., Crawford, C.J., Masek, J.G., Woodcock, C.E., Allen, R.G., Anderson, M.C., Belward, A.S., Cohen, W.B., Dwyer, J., Erb, A., Gao, F., Griffiths, P., Helder, D., Hermosilla, T., Hipple, J.D., Hostert, P., Hughes, M.J., Huntington, J., Johnson, D.M., Kennedy, R., Kilic, A., Li, Z., Lymburner, L., McCorkel, J., Pahlevan, N., Scambos, T.A., Schaaf, C., Schott, J.R., Sheng, Y., Storey, J., Vermote, E., Vogelmann, J., White, J.C., Wynne, R.H., Zhu, Z., 2019. Current status of Landsat program, science, and applications. Remote Sens. Environ. 225, 127–147. https://doi.org/10.1016/j.rse.2019.02.015.

Wulder, M.A., Roy, D.P., Radeloff, V.C., Loveland, T.R., Anderson, M.C., Johnson, D.M., Healey, S., Zhu, Z., Scambos, T.A., Pahlevan, N., Hansen, M., Gorelick, N., Crawford, C.J., Masek, J.G., Hermosilla, T., White, J.C., Belward, A.S., Schaaf, C., Woodcock, C.E., Huntington, J.L., Lymburner, L., Hostert, P., Gao, F., Lyapustin, A., Pekel, J.-F., Strobl, P., Cook, B.D., 2022. Fifty years of Landsat science and impacts. Remote Sens. Environ. 280, 113195 https://doi.org/10.1016/j.rse.2022.113195.

Wulder, M.A., White, J.C., Loveland, T.R., Woodcock, C.E., Belward, A.S., Cohen, W.B., Fosnight, E.A., Shaw, J., Masek, J.G., Roy, D.P., 2016. The global Landsat archive—status, consolidation, and direction. Remote Sens. Environ. 185, 271–283. https://doi.org/10.1016/j.rse.2015.11.032.

Yan, L., Roy, D.P., 2021. Improving Landsat Multispectral Scanner (MSS) geolocation by least-squares-adjustment based time-series co-registration. Remote Sens. Environ. 252, 112181 https://doi.org/10.1016/j.rse.2020.112181.

Yan, L., Roy, D.P., 2020. Spatially and temporally complete Landsat reflectance time series modelling: the fill-and-fit approach. Rem. Sens. Environ. 241, 111718.

Zhai, Y., Roy, D.P., Martins, V.S., Zhang, H.K., Yan, L., Li, Z., 2022. Conterminous United States Landsat-8 top of atmosphere and surface reflectance tasseled cap transformation coefficients. Remote Sens. Environ. 274, 112992 https://doi.org/10.1016/j.rse.2022.112992.

Zhang, H.K., Roy, D.P., 2016. Landsat 5 Thematic Mapper reflectance and NDVI 27-year time series inconsistencies due to satellite orbit change. Remote Sens. Environ. 186, 217–233. https://doi.org/10.1016/j.rse.2016.08.022.

Zhang, H.K., Roy, D.P., Yan, L., Li, Z., Huang, H., Vermote, E., Skakun, S., Roger, J.-C., 2018. Characterization of Sentinel-2A and Landsat-8 top of atmosphere, surface, and nadir BRDF adjusted reflectance and NDVI differences. Remote Sens. Environ. 215, 482–494. https://doi.org/10.1016/j.rse.2018.04.031.

Zhang, H.K., Roy, D.P., Luo, D., 2023. Demonstration of large area land cover classification with a one dimensional convolutional neural network applied to single pixel temporal metric percentiles. Remote Sens. Environ. 295, 113653 https://doi.org/10.1016/j.rse.2023.113653.

Zhu, Z., Wang, S., Woodcock, C.E., 2015. Improvement and expansion of the Fmask algorithm: cloud, cloud shadow, and snow detection for Landsats 4–7, 8, and Sentinel 2 images. Remote Sens. Environ. 159, 269–277. https://doi.org/10.1016/j.rse.2014.12.014.

Zhu, Z., Woodcock, C.E., 2012. Object-based cloud and cloud shadow detection in Landsat imagery. Remote Sens. Environ. 118, 83–94. https://doi.org/10.1016/j.rse.2011.10.028.

Zhu, Z., Wulder, M.A., Roy, D.P., Woodcock, C.E., Hansen, M.C., Radeloff, V.C., Healey, S.P., Schaaf, C., Hostert, P., Strobl, P., Pekel, J.-F., Lymburner, L., Pahlevan, N., Scambos, T.A., 2019. Benefits of the free and open Landsat data policy. Remote Sens. Environ. 224, 382–385. https://doi.org/10.1016/j.rse.2019.02.016.